

MONITORING GLOBAL SEA LEVEL: EUSTATIC VARIATIONS, LOCAL  
VARIATIONS, AND SOLID EARTH EFFECTS

Grant NAG5-6068

Final Report

For the Period 15 July 1997 through 14 July 2000

Principal Investigator

Dr. James L. Davis

December 2000

Prepared for

National Aeronautics and Space Administration  
Goddard Space Flight Center, Greenbelt, MD

Smithsonian Institution  
Astrophysical Observatory  
Cambridge, Massachusetts 02138

<p>The Smithsonian Astrophysical Observatory is a member of the Harvard-Smithsonian Center for Astrophysics</p>
---



## I. Introduction

This project involves obtaining GPS measurements in Scandinavia, and using the measurements to correct tide-gauge measurements for the rebound effect and to estimate the viscosity profile of the Earth's mantle. Below, we report on several aspects of this project.

## II. GPS Measurements

The BIFROST permanent networks set up by Onsala Space Observatory and the Finnish Geodetic Institute continues to operate, and the data are continuously being analyzed.

The planned analysis of the BIFROST GPS data was carried out. In March, we produced a new velocity solution.

## III. Geodetic and Geophysical Results

These have been reported in a recent submission to JGR, Continuous GPS measurements of post-glacial adjustment in Fennoscandia, 1. Geodetic results. This manuscript is attached as Appendix A.

## IV. Sea Level and Postglacial Rebound WWW Site

This site has been down since May 30 for extensive remodeling. We are implementing our post-glacial rebound calculator with several hundred possible model combinations.

## **Appendix A**

Attached is the paper submitted to the Journal of Geophysical Research in April, 2000: Continuous GPS measurements of postglacial adjustment in Fennoscandia, 1. Geodetic results.

## **Continuous GPS measurements of postglacial adjustment in Fennoscandia, 1. Geodetic results**

J. M. Johansson,<sup>1</sup> J. L. Davis,<sup>2</sup> H.-G. Scherneck,<sup>1</sup> G. A. Milne,<sup>2,3</sup> M. Vermeer,<sup>4</sup> J. X. Mitrovica,<sup>5</sup> R. A. Bennett,<sup>2</sup> B. Jonsson,<sup>6</sup> G. Elgered,<sup>1</sup> P. Elósegui,<sup>2</sup> H. Koivula,<sup>4</sup> M. Poutanen,<sup>4</sup> B. O. Rönnäng,<sup>1</sup> and I. I. Shapiro<sup>2</sup>

Short title: FENNOSCANDIAN GPS: GEODETIC RESULTS

**Abstract.** Project BIFROST (Baseline Inferences for Fennoscandian Rebound Observations, Sea-level, and Tectonics) combines networks of continuously operating GPS receivers in Sweden and Finland to measure ongoing crustal deformation due to glacial isostatic adjustment (GIA). We present an analysis of data collected in the years 1993–1998. We compare the GPS determinations of three-dimensional crustal motion to predictions calculated using the high resolution Fennoscandian deglaciation model recently proposed by *Lambeck et al.* [1998a,b]. We find that the the maximum observed uplift rate ( $\sim 10 \text{ mm yr}^{-1}$ ) and the maximum predicted uplift rate agree to better than  $1 \text{ mm yr}^{-1}$ . The patterns of uplift also agree quite well, although differences are discernible. The  $\chi^2$  difference between predicted and GPS-observed radial rates is reduced by a factor of 5–6 compared to that for the “null” (no uplift) model, depending on whether a mean difference is first removed. The north components of velocity agree at about the same relative level, whereas the agreement for the east components is worse, a problem possibly related to the lack of bias fixing. We have also compared the values for the observed radial deformation rates to those based on sea-level rates from Baltic tide gauges. The weighted RMS difference between GPS and tide-gauge rates (after removing a mean) is  $0.6 \text{ mm yr}^{-1}$ , giving an indication of the combined accuracy of the GPS and tide-gauge measurement systems. Spectral analysis of the time series of position estimates yields spectral indices in the range  $-1$  to  $-2$ . An EOF analysis indicates, however, that much of this power is correlated among the sites. The correlation appears to be regional and falls off only slightly with distance. Some of this correlated noise is associated with snow accumulation on the antennas or, for those antennas with radomes, on the radomes. This problem has caused us to modify the radomes used several times, leading to one of our more significant sources of uncertainty.

## 1. Introduction

The last 800 ka of the current ice age have been characterized by a series of “glacial cycles,” each with a period of approximately 100 kyr [e.g., *Broecker and van Donk*, 1971]. Within each cycle a relatively slow glaciation phase, culminating in massive ice complexes over most of the high latitude continental regions, was followed by a much more rapid deglaciation event. For example, during the last glacial maximum, which occurred just  $\sim 20$  kyr B.P., the ice sheets reached thicknesses of 2–3 km or more in Fennoscandia, Canada, Antarctica, Greenland, Siberia, and Arctic Canada [*Denton and Hughes*, 1981]. Remarkably, in a matter of only 15 kyr, a large proportion of ice disintegrated, leaving most of these regions ice-free and raising world-wide ocean levels by over 100 m [e.g., *Chappell and Shackleton*, 1986]. The redistribution of surface ice-water mass implied by these glaciation/deglaciation episodes has induced an appreciable and ongoing isostatic adjustment of the planet.

Glacial isostatic adjustment (GIA) is manifested in a wide variety of past- and present-day geophysical observables that have previously been used to study this process, including time series of ancient sea-level elevations (relative to present-day sea level), the modern tide gauge record, gravity anomalies, present-day secular variations in the global gravity field, and present-day secular variations in the Earth’s rotational state (variations in length of day and motion of the rotation pole) [e.g., *Milne*, 1998]. These observations provide an indirect inference of present-day ongoing crustal deformation. Direct high-accuracy measurements of crustal deformation, even in a particular region, were not possible, however, before the advent of space geodetic techniques, and even these techniques have only quite recently been able to achieve the required accuracy. Very long baseline interferometry (VLBI) has been available as a high-accuracy geodetic technique for over 20 years; several studies have now addressed the effects of GIA on VLBI determinations of site velocities [e.g., *James and Lambert*, 1993; *Mitrovica et al.*, 1993]. Unfortunately, the global VLBI network is extremely sparse, and only 2–3 sites

exhibit much sensitivity to GIA. A small error in the velocity determination of these sites will unduly influence conclusions regarding mantle viscosity and ice-sheet histories [Mitrovica *et al.*, 1993; Mitrovica *et al.*, 1994b].

Geodesy with the Global Positioning System (GPS) affords us several advantages relative to geodesy with VLBI related to the relatively low cost of the GPS receivers (~\$15 K or less). As a result of this low cost it is feasible to deploy a dense network of receivers across a region. The detailed pattern of deformation may thus be inferred. The low cost of GPS receivers moreover makes it financially feasible to dedicate a group of GPS receivers to “permanent” sites within a region in order to acquire “continuous” measurements. In principle, given sources of error that are sufficiently steady state, it should be possible to “beat down” the noise and thus determine estimates of velocity much more quickly and accurately than with conventional “campaign” GPS measurements. The number of GPS receivers in permanent GPS networks is quickly outpacing the number used for conventional campaign high-accuracy geodetic measurements [e.g., Segall and Davis, 1997].

Geodesy with GPS has been steadily and significantly improving in precision and accuracy over the past ten years. This improvement has mainly been due to advances in the GPS satellite constellation, GPS receiver design, and analysis techniques. The demonstrated repeatability of horizontal position estimates obtained from GPS is currently at the few-mm level on regional and local scales and at the 10-mm level on global scales [e.g., Blewitt, 1993]. The repeatability in the vertical baseline component is typically 3–5 times worse. The level of accuracy achievable in a single day with the GPS technique is thus in principle equal to that achievable with VLBI.

In August 1993, we established a network of permanently operating GPS receivers in Sweden [BIFROST Project, 1996]. A number of sites in Finland were also temporarily occupied. In 1994–6, permanent GPS sites were established in Finland. The GPS sites within these networks, along with several already existing sites of the International GPS

Network for Geodynamics (IGS) sites in Norway operated by the Norwegian Mapping Authority, make up a dense regional Fennoscandian GPS network of an intersite spacing of  $\sim 100$  km and a total area of  $\sim 2000 \times 2000$  km, situated within the area covered by ice at the last glacial maximum. Investigators from three Nordic and two North American institutions formed Project BIFROST (Baseline Inferences for Fennoscandian Rebound, Sea level, and Tectonics) [*BIFROST Project*, 1996]. One of the primary goals of BIFROST is to use the three-dimensional velocity vectors from the BIFROST GPS network to provide a new GIA observable for the determination of Earth structure and Fennoscandian ice history. In this paper, we report on the first results from this effort. We will present the BIFROST GPS networks and data sets, and describe the analysis of the GPS data. We include a thorough discussion of errors since the GIA signals we are attempting to measure are quite small (sub-cm).

## 2. The BIFROST GPS Networks

The BIFROST GPS networks (Figure 1) are composed of the permanent GPS networks of Sweden (SWEPOS<sup>TM</sup>) and Finland (FinnRef). Table 1 describes the histories of the BIFROST sites. This table contains the dates and configurations of the original installations, as well as the dates on which significant modifications were made to the site hardware. (Minor changes, such as those affecting communication only, are not indicated in Table 1.) The hardware described in Table 1 includes the GPS receiver type, GPS antenna type, radome type, monument type, and approximate positions. IERS Domes Numbers for those sites which are IGS sites are given as well.

Below, we discuss the individual aspects of both BIFROST networks.

### 2.1. The SWEPOS GPS Network

The Swedish nationwide multipurpose network of twenty-four permanent GPS stations, SWEPOS, was established in 1993. On July 1, 1998, SWEPOS attained

full operational capability for real-time positioning at the meter accuracy and for post-processing applications with centimeter accuracy. Real-time positioning at the centimeter/decimeter level is planned for 2002. The National Land Survey of Sweden (LMV) is responsible for the maintenance and the operation of the SWEPOS network

The SWEPOS network (Figure 1) currently consists of 21 continuously operating GPS stations. The "standard" SWEPOS monument (designed by the LMV and denoted as "SWEPOS" in Table 1) consists of a 3-m tall concrete circular pillar atop a concrete platform. At five sites (Kiruna, Lovö, Mårtsbo, Norköping, and Skellefteå) a second pillar is available to serve as an alternate and as a platform for test measurements. The pillars are built on bedrock and the line of sight from the top to the GPS satellites is unblocked at elevation angles above  $10^\circ$  and often lower. Each pillar is supported by four internal steel rods set 1 m into the underlying rock. Heating coils are helically around each concrete pillar. Insulating material consisting of helically wound corrugated plastic sheet and rockwool surrounds the wire-wrapped pillar. A temperature sensor is fit into a small cavity inside the pillar and is connected to a thermostat unit in the instrument cabin. The thermostat maintains the temperature of the sensor above  $15^\circ\text{C}$ . On the top of each pillar is a plate for the attachment of the GPS antenna, tribrach, and adaptor.

The pillars at each site are surrounded by a network of steel pins, driven into the rock so that their tops protrude a few centimeters above the surface. This local network, covering an area of approximately  $15\text{ m} \times 15\text{ m}$ , is used to monitor the stability of the concrete pillars. The GPS antenna is removed from the pillar and replaced with a theodolite, which is used to measure the horizontal and vertical angles to the steel pins. Through resection the position of the pillar can be calculated. In this manner, the local position and orientation of the pillar may be monitored to better than 1 mm. The first such measurements were obtained during summer 1993 and repeated annually except for the monument in Leksand where measurements are carried out monthly. The results of these measurements are described below.

Several sites have slight variations in monumentation. The Onsala site has a different monument, due to its earlier construction as an IGS site. The Onsala monument consists of a 1 m tall pillar with a square cross-section and without heating control or insulating material. The Jönköping pillar is 1 m shorter than the standard pillar (for air traffic safety), and also is not heated. The Lovö and Mårtsbo monuments are SWEPOS monuments built over pre-existing pillars of rectangular cross-section. In addition, the multipath environment at these two station might be worse than at others due to pre-existing construction.

Each SWEPOS site has a 3 m × 2 m hut housing the GPS receivers, backup batteries, computer, and Internet connection. All SWEPOS sites are equipped with two or more GPS receiver systems, and AOA SNR-8000 and an Ashtec Z-XII, connected to a single Dorne-Margolin type antenna. At four stations dual-frequency GPS/GLONASS receivers are also installed. The stations are equipped with a power backup system, which can run the station for 48 hours if the main power fails. All stations are connected to the control center via leased 64 kbit lines and a redundant 19.2 kbit X.25 line.

## **2.2. The FinnRef GPS Network**

Planning for the FinnRef network (Figure 1) started at the Finnish Geodetic Institute (FGI) at the end of 1992, when it was decided that a network of 12 stations would be established. Possible site candidates were chosen with several criteria in mind: (1) the network should cover the country so that the maximum land uplift differences could be sampled; (2) the stations should be built on bedrock and there should be open sky above an elevation angle of 15°; (3) absolute gravity has been or can be measured on the spot; and (4) stations should easily be connected to the precise levelling network and to the telephone and electricity networks. The criterion (2) has generally, but not universally, been met, and in most cases the horizon is 10° or lower. Planning, construction and use of the network are described in more detail elsewhere [e.g., *Koivula*

*et al.*, 1997, 1998]

At the Joensuu, Kuusamo, Vaasa, Virolahti, Olkiluoto, Kivetty and Romuvaara stations we constructed heated wooden cabins of area 1.5–2 m × 3 m to house the GPS and other electronics. Existing buildings were used at all other sites.

Some stations are located close to other institutions where on-site personnel can assist in case of minor problems. Kevo is on the premises of the Subarctic Research Center of the University of Turku, Oulu is at the Aarne Karjalainen Observatory of the University of Oulu; Sodankylä is visited weekly by local staff of the Sodankylä Geophysical Observatory; and Tuorla is at the Astronomical Observatory of the University of Turku. At Kivetty, Olkiluoto and Romuvaara there are also contact persons who can check the stations. Metsähovi is at the Space Geodetic Observatory of the FGI.

Three different types of antenna platforms are used for FinnRef. The standard configuration is a 2.5 m high steel grid mast, which is used at Joensuu, Kuusamo, Sodankylä, Tuorla, Vaasa and Virolahti. A similar mast, but 5 m high is used at Kevo. In the case of the 2.5 m mast, the thermal expansion effects amount to a height variation of less than  $\pm 1$  mm during the annual temperature cycle. This variation is considered to be acceptable. Around the antenna masts, there are three reference bench marks, and connections to the first order levelling network have also been established.

Two stations have higher masts. There is an anchored 25 m high steel grid mast at Metsähovi and at Oulu there is a cylindrical 8 m steel mast. In both cases the height of the GPS antenna is stabilized with an invar rod. The antenna is isolated from the mast with an attachment piece and a spring system, which is anchored to the bedrock with an invar rod or wire [*Paunonen*, 1993]. The system for Oulu was adapted from that at Metsähovi. Three stations, Olkiluoto, Kivetty and Romuvaara, were built in cooperation with Posiva Oy, a company which is responsible for locating sites for disposal of nuclear waste. Local networks around these sites are remeasured semiannually in order to locate

possible deformations. For this reason more stable concrete pillars were chosen at these sites [*Chen and Kakkuri*, 1994].

All stations are equipped with Ashtech Z-XII GPS receivers, Dorne-Margolin type antennas, modems and power supplies. The exception is Metsähovi where an AOA SNR-8100 receiver is in use. At Metsähovi there is also an external H-maser; at all other stations the receiver's internal oscillator is used. Except Metsähovi and Tuorla, all antennas are equipped with a radome. These have proven less than satisfactory for their stated purpose, but it was decided not to change the antenna mount further due to the experience with SWEPOS.

Data are collected using a sampling interval of 30 s and a 5° elevation-angle cut-off. During the 1998/9 winter CB00 software was installed into all receivers and the sites were equipped with Vaisala PTU 220 meteosensors. The station histories are summarized in Table 1.

### **3. Data Analysis and Geodetic Results**

The dual-frequency GPS phase and pseudorange data were processed using the 2nd release of GIPSY software developed at Jet Propulsion Laboratory (JPL) [e.g., *Webb and Zumberge*, 1993]. Dual-frequency phase and pseudorange data from a single 30-hour period acquired from all the sites in the network are analyzed simultaneously. (There is a 3-hour overlap at each end of each observing session.) The GPS data are decimated to achieve an effective sample rate of 300 sec; decimation is performed to maintain a manageable level of utilized disk space. For each 30-hour data set we estimated the usual set of parameters, including oscillator ("clock") corrections, site positions, atmospheric zenith delay parameters, and ambiguity parameters. Satellite orbit parameters were highly constrained to the values distributed by the IGS based on a solution involving a global network of GPS sites. Temporal variations in the clock and atmosphere parameters are modeled as independent random walks [*Webb and Zumberge*,

1993]. We adopted a minimum elevation angle of  $15^\circ$  for all stations. Corrections for the motion associated with ocean loading and solid-Earth tides were incorporated in the model.

For the SWEPOS sites, which now have multiple antennas, the SNR-8000 data are used in the solution up until August 1, 1998, and the Z-XII data thereafter. For a period following this date we performed a number of solutions with both GPS receivers and determined differences at the 1 mm level or less.

We adopted the value of 10 mm for the uncertainties in the phase measurements at each frequency. The instrumental uncertainties for such measurements are much smaller, perhaps 1–3 mm [Spilker, 1996]. However, experience within the GPS community has shown that the scatter of the time series is greater than the theoretical value based on instrumental noise only. The increase in the scatter above the predicted value can of course be attributed to unmodeled phase variations, which may or may not have a white noise (or nearly white noise) nature. In Section 5 we discuss a number of errors which might contribute to this increased scatter, and we investigate the spectral characteristics of the site position variations. It is important to remember throughout the paper, though, that the uncertainties for the estimated parameters, including site position and therefore velocity and geophysical parameters, are approximations.

Data processing utilizes a “no-fiducial” technique described by *Heflin et al.* [1992] wherein station coordinates have weak a priori constraints. The results presented in the following sections were achieved without fixing the estimated phase biases to integer values, since the software cannot handle automatically such an extensive data set. Independent tests with a smaller data set (SWEPOS stations only) have shown that “bias fixing” leads to a decrease in the formal errors of about 20–30%.

All geodetic positions obtained in the GIPSY analysis are finally transformed into the International Terrestrial Reference Frame of 1996 (ITRF96) [Sillard *et al.*, 1998]. This transformation creates a slight inconsistency since the satellite orbits prior to

September 1996 are referred to different editions of ITRF (ITRF92 until July 1994, ITRF93N until June 1995, and ITRF94 until September 1996). The problem that concerns us here is that the frames have slightly different net rotations and translations. Using a set of core stations constituted by those that are jointly present in pairwise successive reference frames and applying weights as given by the velocity uncertainties, the rotations and translations derived by least-squares adjustment can amount to  $1 \text{ mm yr}^{-1}$  at the Earth's surface in any component. We have therefore estimated and applied the inter-frame rotation and translation parameters to correct the time series of station positions for these biases. The results are thus determined in a rigid frame that is co-moving with the ITRF96 frame, which for our sites is dominated by the ITRF96 realization of the Eurasian plate motion. We, however, are interested in deformations relative to the Eurasian plate motion.

Removing the motion of the Eurasian plate requires a decision regarding the type of motion the co-moving Eurasian frame should be allowed. The requirement to observe deformation from a rigid co-travelling frame implies the need to suppress a deformation mode conveyed by a scale rate parameter. Although any residual rotation in one corner of the region could easily be corrected for by adding small rigid rotations, the case is slightly more intricate when one simultaneously considers translations. Considering horizontal motion, the virtue of the GPS data in application to GIA lies in the ability to resolve intersite motions; subtracting the motion of a rigid frame will have no influence on relative deformation. In the case of radial motions, GPS data will not only be used to study relative deformation, but also offers the prospect of studying the vertical motion of the crust, for example, in comparison with the sea surface. An “absolute” frame is therefore desired.

Allowing for translations in the co-moving frame will effect the estimates of vertical components of site motion. One could argue that the European stations are well established and stable, so that the ITRF96 motion after correction for vertical motion

from one or a set of models would provide a proper regional vertical reference. The associated co-moving frame would be constructed by estimating rotation and translation rate parameters using the subset of velocity estimates at those European IGS stations that also were used in the projection stage.

On the other hand, the large number of stations world-wide now included in the ITRF should provide a stable constraint. In the larger, global set, local vertical motion will appear as less correlated. Accepting this argument, the consequence is to not allow relative vertical motion between the co-moving frame and the ITRF, i.e., use only the horizontal projection of the ITRF site motion vectors. This method brings about an advantage, namely that the observed data do not have to be “corrected” with a model, thereby avoiding problems of circular arguments at the stage where the network rates are interpreted. The associated co-moving frame is simply constructed by solving for rotation rates only. We have therefore adopted this method.

The analysis described above yields a time series for each station of three-dimensional position in the ITRF96 “Eurasia co-moving” reference frame. Time series for the BIFROST stations and Tromsø, a nearby IGS site, are shown in Figure 2.

### **3.1. Antenna-Related Issues**

Several of the time series in Figure 2 for sites of the SWEPOS network exhibit one or more “jumps.” We do not believe that these jumps represent motions of the GPS antenna. The jumps are associated with (1) removal and replacement of the GPS antennas, (2) changes in antenna radomes, and (3) rapid changes in snow accumulation. Snow accumulation is discussed in Section 5.4.

In the removal and replacement of the GPS antennas to perform the local site surveys mentioned above, the GPS antenna is positioned on the monument by means of a threaded hole and a standard 5/8” surveyor’s bolt attached to a metal plate that has been permanently set into the concrete at the top of the pillar. The GPS antenna

is screwed onto the bolt until it refuses to rotate. When the antennas are removed and replaced, the orientation of the antenna is checked to insure that it is the same as before removal. Given that the surveyor's bolt has 5 threads per inch, a rather large orientation error of  $45^\circ$  would lead to a vertical displacement of only 0.6 mm, and to no horizontal displacement. The "jumps" in Figure 2 associated with these surveys, on the other hand, can be at the 10 mm level.

A likely explanation for these jumps is that very small differences in antenna orientation lead to changes in phase errors because of electromagnetic coupling [*Elósegui et al.*, 1995; *Jaldehyag et al.*, 1996b] and antenna phase center variations [*Schupler et al.*, 1994]. Both these sources of error are potentially elevation- and azimuth-angle dependent, and in the case of the former the position relative to the pillar and metal plate is critical. If one imagines that the phase errors induced by these two phenomena can be represented as a series of spherical harmonics, with angular arguments of azimuth and elevation angles, then the contribution from the  $\ell = 1$  term is indistinguishable from the contribution to phase variations from a site position offset.

Other apparent jumps occur when there were changes in the antenna radomes. The original radomes installed on the SWEPOS sites were designed at Delft University of Technology. During the winter of the first year of the experiment, snow accumulated significantly on these radomes, and our observations led us to believe that this accumulation could be reduced by a redesigned radome having no horizontal surfaces. Re-designed radomes ("Type A") were emplaced in the winter and spring of 1995. We later discovered that the paint process used on these radomes were defective. These radomes were thus removed in the spring and summer of 1996 and later that year replaced with improved radomes ("Type B"). Each of these changes appears to produce offsets in the time series. The radomes are discussed in detail by *Emardson et al.* [2000].

As an ad hoc treatment for these errors, we have simply estimated three-dimensional offsets in position on the epochs at which radomes were changed, the GPS antennas

removed and replaced, or the antenna rotated. These changes are summarized in Table 1. The site velocity was assumed to be constant for the entire experiment. This ad hoc procedure is not very satisfying, since the existence of the offsets is an indication of an error source which could conceivably have a temporal variation and therefore could effect the estimate of the rate.

### 3.2. Determination of Station Velocities

In this section, we report and compare several methods for determining the station velocities. Since, after the analysis described above, the time series of station positions are in a consistent reference frame, it is in principle simply a matter of fitting a straight line component by component and site by site to the time series. This method does not yield determinations of the correlations of the errors in the rate estimates, but these are formally very small since the orbit parameters were highly constrained in the original solutions. In order to gain a quantitative understanding of the effects of errors that are difficult or impossible to model, we present several different analyses for the rates. Each analysis uses different models for the variation of site position with time as well as different editing criteria.

In the following, the standard deviations we report are the so-called “standard errors.” These standard errors are based on the phase uncertainties used in the daily least-squares analysis, described above, propagated through that analysis to yield standard deviations for daily determinations. (The standard errors are the uncertainties shown in Figure 2.) The errors for estimates obtained on different days are assumed to be uncorrelated. These standard deviations are then propagated through the analyses described below to yield the standard errors for the rate parameters. In general, the reduced  $\chi^2$  postfit residuals are close to unity, indicating a reasonable fit, but this statistic may not be an accurate measure of the accuracy of the rate estimates. In the next section, we assess these standard errors and the accuracy of the rate estimates.

The solutions for the three-dimensional crustal deformation velocities and their standard errors for the different analyses are presented in Table 2. In all cases data prior to 1998.0 only were used. Below, we describe the different solutions.

**3.2.1. Standard solution.** In the “standard solution,” sites having a short time series are analyzed differently from those having a longer time series. For longer time series (generally those with a timespan of two years or greater), the model for the position estimates included: a mean value, a constant rate, an admittance parameter for atmospheric loading [*vanDam and Wahr, 1993*], and periodic terms with frequencies of one, two, and three cycles per year. (The periodic terms are meant to model approximately the effects of snow accumulation.) For the short time series, no periodic terms were included. For the radial (“up”) components only, offsets at each antenna change (Table 1) were included. No editing was performed.

**3.2.2. Edited solution.** The parameterization is identical to the standard analysis, with the following exceptions. No difference was drawn between short and long time series. No admittance parameters for atmospheric loading were estimated, and the annual periodic term only was included. Offsets for antenna changes were estimated for all components. An editing loop was included that deleted data whose postfit residual was greater than three times the weighted root-mean-square (WRMS) residual. This loop was repeated three times. Data from time periods 1995.000–1995.104, 1995.370–1995.520, and 1996.438–1996.616 were automatically deleted. These periods represent timespans during which radome change/replacement was occurring across the network.

**3.2.3. EOF solution.** An empirical orthogonal function (EOF) analysis for the radial rates was performed on a subset of the data. This analysis is described fully in Section 5.1. Table 2 includes the radial rates resulting from this solution.

### 3.3. Comparison of Solutions

In Figure 3 we have compared rate determinations for all three components for the Standard and Edited solutions, and the radial rates for the EOF solution. In general the agreement is quite good despite the differences between these analyses, but in several cases the disagreement is quite large. Generally, the extreme differences occur for rates with larger error bars, indicating a shorter time series. Thus, these rates are relatively less stable to changes in analysis strategy. An obvious and important exception to this observation is the rate determination for Kiruna. From Table 2, we see that the radial rate for this site from the Standard solution is  $11.7 \pm 0.9$  mm yr<sup>-1</sup>, whereas the rate from the EOF solution is  $10.6 \pm 1.9$  mm yr<sup>-1</sup> and the rate from the Edited solution is  $4.7 \pm 0.9$  mm yr<sup>-1</sup>. Kiruna, a site in the north of Sweden, has a great deal of snowfall. The average winter precipitation is over 100 mm with an average winter temperature of approximately  $-10$  °C [Schönwiese and Rapp, 1997]. Kiruna was the site at which snow accumulation was first noticed, and it has some of the largest seasonal signatures (Figure 4). Furthermore, only in the latest period has Kiruna had more than one continuous year of data with no offsets (Figure 2). Thus, Kiruna may be the most outstanding example of the types of problems discussed above.

The differences between the Standard and Edited solutions have WRMS differences of  $0.9$  mm yr<sup>-1</sup> (east),  $0.5$  mm yr<sup>-1</sup> (north), and  $1.6$  mm yr<sup>-1</sup> (radial). Treated as independent solutions of equal weight, this would indicate a typical uncertainty for a single rate of  $0.6$  mm yr<sup>-1</sup> (east),  $0.4$  mm yr<sup>-1</sup> (north), and  $1.1$  mm yr<sup>-1</sup> (radial). This represents a scaling of the typical standard errors of 3–4 for the horizontal components and 1.5 for the radial. However, these solutions are not independent and in fact use much the same data set. From this point of view, the differences between the standard and edited solutions are large.

The accuracy of the rates estimates cannot be perfectly assessed by a comparison like that of Figure 3, since the analyses share overlapping data sets and thus the

comparisons will not reveal common errors. Nevertheless, Figure 3 gives us an indication of the shortcomings in our modeling of the time series. By comparing to models for crustal deformation, we can obtain a rough assessment of our errors, and this comparison is contained in Section 4. Sources of error other than those discussed above are analyzed in Section 5. Phenomena that may actually influence the position of the site are considered also in Section 4. A more complete understanding of our errors will come with longer time series having no equipment changes are established.

## 4. Interpretation of Observed Deformation Rates

As stated above, a primary goal of the BIFROST Project is to provide a new and useful GIA observable with which to constrain models of the GIA process in Fennoscandia. In order to achieve this goal, the observations must exhibit a coherent signal that is clearly related to the regional GIA process. In this section we test this requirement by comparing the observed three-dimensional deformation rate signal to numerical predictions of this field and to the apparent sea-level signal that has long been associated with the GIA process. We also consider several other geophysical effects that may produce temporal variations in site position.

### 4.1. Glacial Isostatic Adjustment

A number of publications, some dating back to the 1930's [e.g., *Haskell*, 1935; *Vening Meinesz*, 1937], have employed sea-level observations to infer Earth viscosity and ice sheet parameters in the Fennoscandian region [e.g., *Fjeldskaar*, 1994; *Mitrovica*, 1996; *Lambeck et al.* 1998a; *Davis et al.*, 1999]. In the recent study of *Lambeck et al.* [1998a], a three-layer Earth viscosity model and a regional ice model were proposed that provide a good fit to a carefully compiled and extensive data set based on geological sea-level markers. The preferred Earth models are defined by a lithospheric thickness of 65–85 km, an upper mantle viscosity of  $3\text{--}4 \times 10^{20}$  Pa s and a lower mantle viscosity

that is a factor of ten or more greater than the upper mantle value. This range of three-layer Earth models and ice model were also found to produce a good fit to recent instrumented sea-level and lake-level records [*Lambeck et al.*, 1998b]. (This more recent, shorter time-scale data apparently did not allow a robust inference of lower mantle viscosity.)

A number of previous inferences that appear to disagree with the above described viscosity profile [e.g., *Wolf*, 1987; *Fjeldskaar*, 1994] are, in fact, found to be compatible when the resolving depth of the various data sets is considered [*Mitrovica*, 1996]. The inference of *Mitrovica and Peltier* [1993], which is based on the so-called Fennoscandian relaxation spectrum [*McConnell*, 1968], is not consistent with the *Lambeck et al.* [1998a] result. However, recent studies show that the paleoshoreline data upon which this spectrum is based require some revision [*Wolf*, 1996]. Indeed, a recent re-analysis of the spectrum was found to eliminate the inconsistency [*Wieczerkowski et al.*, 1999] between these two inferences. We have limited the above discussion to recent GIA analyses that considered data from north western Europe. We have not considered recent analyses based on global sea-level data sets (which may include data from north western Europe) in order to avoid the potential bias introduced to these inferences from lateral variations in viscosity structure.

The following predictions are based on a spherically symmetric, compressible, Maxwell viscoelastic Earth model. We choose a three-layer viscosity model defined by a lithospheric thickness of 70 km, an upper mantle of  $4 \times 10^{20}$  Pa s and a lower mantle viscosity of  $5 \times 10^{21}$  Pa s. (These values are consistent with the sea-level constraints discussed above.) The elastic structure of our Earth model is taken directly from the seismically constrained PREM [*Dziewonski and Anderson*, 1981]. The ocean component of the surface load is computed via a revised sea-level algorithm that solves the sea-level equation [*Farrell and Clark*, 1976] in a gravitationally self consistent manner while incorporating the effects of GIA-induced perturbations to the Earth's

rotation vector [e.g., *Milne*, 1998] and the postglacial influx of ocean water/meltwater to once-ice-covered regions [*Milne*, 1998]. Predictions of the load-induced three-dimensional deformation rate signal are calculated via the theory of *Mitrovica et al.* [1994a]. This theory has also been extended to incorporate the influence of GIA-induced perturbations in the Earth’s rotation vector *Mitrovica et al.* [2000]. The relative importance of the different components of the model will be described in a future publication.

We require an ice model that provides a good fit to the sea-level observations for our choice of Earth model. This criterion is met by the model proposed by *Lambeck et al.* [1998a]. However, in order to accurately solve the sea-level equation and realistically compute GIA-induced perturbations to the Earth’s rotation vector, we require a global ice model. To meet both of these requirements we remove the Fennoscandian and Barents Sea components of the lower resolution, global ICE-3G [*Tushingham and Peltier*, 1991] model and replace these by the high resolution, regional model proposed by *Lambeck et al.* [1998a]. The contours of uplift that we calculate using this ice model and the Earth model described above are shown in Figure 4a.

In order to illustrate the pattern of uplift that we observe from the BIFROST network, we have fit a simple surface to the vertical rates from the standard solution. The model we have chosen for the radial rate  $\dot{u}$  at longitude  $\lambda$  and latitude  $\phi$  is a two-dimensional Gaussian model:

$$\dot{u}(\lambda, \phi) = \dot{u}_o + \dot{u}_a \exp \left[ - \left\{ w_1^2 (\lambda - \lambda_o)^2 + w_2 (\lambda - \lambda_o) (\phi - \phi_o) + w_3^2 (\phi - \phi_o)^2 \right\} \right] \quad (1)$$

The Gaussian is centered at  $(\lambda_o, \phi_o)$  and has maximal value  $\dot{u}_o + \dot{u}_a$  and minimal value  $\dot{u}_o$ . The parameters  $w_1$  and  $w_3$  control the widths of the Gaussian and  $w_2$  controls the “tilt” of its primary axis with respect to the north direction. (By choosing this function we do not mean to assert that the uplift should in fact be Gaussian. We are simply using this method to present the observed vertical rates.) In fitting for the seven parameters of the model, we have used for the observation uncertainties  $\sqrt{\sigma_u^2 + \sigma_o^2}$ , where  $\sigma_u$  is the

standard error of the uplift (see above) and  $\sigma_o = 0.5 \text{ mm yr}^{-1}$ . This modification is used to reflect the shortcomings of the simple Gaussian model. With this modification, the  $\chi^2$  residual rate per degree of freedom was 6.5, roughly consistent with the scalings found in Section 3.3.

The resulting model is shown in Figure 4b, and it can be seen that GPS-derived model (which we will henceforth refer to as the “observed rates”) shares much in common with the uplift calculated from the Earth/ice model combination (the “model rates”) described above. The estimated center of the uplift for the observed rates ( $\lambda_o = 19.5^\circ$ ,  $\phi_o = 64.2^\circ$ ) is quite close to, though slightly farther south than, the center of uplift for the model rates. The values of the observed and model maximum uplift rates are nearly the same, however. The areas undergoing subsidence for the observed field differ slightly from those for the model rates, but these areas are outside of the network and good agreement is not to be expected. Finally, the orientation and the amount of elongation agree quite well, although the model deformation is not so symmetric as the two-dimensional Gaussian used to represent the observed rates. This comparison is strong evidence that the vertical crustal motions observed with GPS are associated with the GIA process.

A direct comparison between observed rates and those predicted for the Earth/ice model combination described above is shown in Figure 5. The excellent correlation for the radial velocities is clearly evident, as is the correlation for the north components. The east components display less of a correlation, but whether this poor agreement is due to greater scatter in the observed rates or an error in the ice or Earth models is not obvious. The observed rates show a much greater range of values,  $-2$  to  $+3 \text{ mm yr}^{-1}$ , whereas the predicted rates range only from  $-1$  to  $0.5 \text{ mm yr}^{-1}$ .

For the radial velocities, the reduced  $\chi^2$  difference between the observed and model velocities is 14.2, or 11.6 if a mean difference of  $-1.0 \text{ mm yr}^{-1}$  is removed. For the “null” model that predicts zero radial velocity, the reduced  $\chi^2$  is 74.3. Thus, the reduction

compared to the null model is a factor of 5–6.

As a further check on our vertical rates, we compare observed sea-level rates from Baltic tide-gauge data to rates calculated from the Gaussian model. The tide-gauge data consisted of annual averages obtained from the Permanent Service for Mean Sea Level (PSMSL) [Pugh *et al.*, 1987] for tide gauges with timespans of 40 years or longer after 1930. The exception is the tide gauge at Visby, the data for which are not in the PSMSL data base. The sea-level rate  $\dot{s}$  at a tide-gauge located within the Baltic at  $(\lambda, \phi)$  is related to the land uplift  $\dot{u}$  by

$$\dot{s}(\lambda, \phi) = -\dot{u}(\lambda, \phi) + \dot{g}(\lambda, \phi) + \dot{\mu} \quad (2)$$

where  $\dot{g}$  is the rate of change of geoid and  $\dot{\mu}$  is the eustatic sea-level rate. In Figure 6 we have plotted  $\dot{s}$  from tide-gauge rates versus  $\dot{u}$  from our Gaussian fit to the GPS vertical crustal rates. A strong correlation is evident in this figure. In effect, we have used our simple Gaussian model to interpolate the GPS observations to the latitude and longitude of the tide gauges. This correlation is clear evidence of the relationship between the large apparent sea-level rates observed for several centuries in the Baltic and the observed ongoing vertical crustal motions determined from the GPS data. These apparent sea-level rates have long been interpreted as indications of GIA and have even been used to refine Earth and ice models [e.g., Davis *et al.*, 1999; Lambeck *et al.*, 1998b].

We conclude that the secular vertical crustal rates that we observe using the BIFROST GPS data are mainly associated with the ongoing GIA process. Below, we consider some other processes that may also contribute to the observed rates. In a future paper, we will present in greater detail a geophysical analysis of the BIFROST observations.

## 4.2. Ocean Tide Loading

The effects of global ocean tide loading as well as the solid Earth tides are treated at the stage of GPS carrier phase data analysis. These motions are predominantly diurnal and semidiurnal; aiming for one site position estimate per day it appears more advantageous to account for rapid station position variations in the early processing stages rather than having to remove the effects a posteriori.

The ocean loading coefficients were computed with the same method as the one used for the IERS Conventions 1996 [McCarthy, 1996; Scherneck, 1991]. The ocean tide model adopted for the processing is taken from *Le Provost et al.* [1994]. This model does not contain the Baltic Sea, a sea area that is central to our region, and the possible loading effects of which need a careful account and discussion. It is well established that the diurnal and semidiurnal tides in the Baltic Sea are less than 20 mm almost everywhere, and therefore their loading effects are to be expected at only sub-millimeter amplitudes; they can be neglected. The largest seiche-mode of the Baltic Sea, an east-west oscillation involving the Bay of Kiel, the Baltic Proper, and the Gulf of Finland occurs at 36 hr period [Wübbler and Krauss, 1979]. They can be excited by fast passing low-pressure areas. Significant amplitudes are found only in the bays at either end, lasting a couple of days. The existence of these modes argues for including either time-series of water level at—to the least—diurnal if not more rapid sampling rates of near-by tide gauges, or predicted loading effects based on such observations by means of a hydrodynamic model interfaced with an elastic deformation model [Scherneck, 1991].

On the timescale of days to years, the situation for Baltic Sea is radically different. The geometry of the Baltic Sea basin being well enclosed and connected to the open ocean only through narrows in Denmark and between Denmark and Sweden, causes the mass exchange with the world ocean to be retarded. Seasonal variations of the water level can reach  $\pm 0.5$  m as a combined response of the air pressure and wind situation, and due to the role of the Baltic Sea as a large catchment area where precipitation and

evaporation are highly variable on seasonal to interannual timescales.

In order to obtain rough estimates of the impact of variations in the hydrology of the Baltic Sea area on ground deformation we have conducted a simple pilot study. First we assume that GPS monuments, the locations at which we aim to predict vertical crustal motion, are exactly following with the movement of a solid, homogeneous, elastic crust, i.e., we neglect porosity related deformations of soils and surface layers. We then devise a grid of 5 km mesh width covering the area of Sweden, Finland and most of Norway, on which we distinguish type of land and water coverage (a) land, (b) open ocean, (c) Baltic Sea, (d) great lakes, and (e) large hydropower reservoirs. The deformation is modeled using integrated point load Green's functions in the usual way [e.g., *Scherneck*, 1991]. Going through all cases separately, assuming a unit height slab of water in each of the land types, we thus can model admittance coefficients for the impact of loading due to (a) accumulated snow, rain and soil moisture, and (b)–(e) water level variations in each of the bodies. We leave a detailed account of these studies for future publications. Here, we use typical maximum values for the amplitudes of the loading processes in order to get an idea of the importance of the effects. The results are summarized in Table 3.

Residual long-term rates in the water level when limiting the scope to five years can still be as large as  $20 \text{ mm yr}^{-1}$ . Thus, not accounting for these loading affects can offset the estimated GIA rates by  $0.5 \text{ mm yr}^{-1}$ .

### 4.3. Atmospheric Loading

In the EOF mixed regression we model a time-series of atmospheric loading for every station. Previous work on this problem [*vanDam and Wahr*, 1993] showed generally low air pressure admittance at Onsala and small reductions of post-fit  $\chi^2$ . The timescale of the variations in the pressure field is, unlike in the case of ocean tide loading, predominantly in the range of more than one day. Also, the presently available

processing software is not prepared for the input of three-dimensional time series of a priori site displacement information.

We computed the atmospheric loading effect analogously to ocean tide loading, with the major difference being that we assume the loading effect is zero at the bottom of the open ocean assuming an inverse barometric response. Global air pressure fields at  $1^\circ \times 1^\circ$  spatial and 6 hr temporal resolution are obtained from the European Center for Medium-term Weather Forecasting (ECMWF) and convolved with elastic loading Green's functions for vertical and horizontal displacement. Although it can be shown that loading beyond 2000 km distance contributes little to station displacement, we use the entire global field. In this case the global mass balance is easy to maintain, and annual oscillations between the hemispheres do not offset the displacements. We compute an average pressure field for the entire time span in order to subtract the displacement due to the average atmosphere. Thus, for most of the stations a near zero mean for the computed pressure loading time-series is obtained.

In the eigenvector analysis the air pressure loading information that is orthogonal to the station residuals is retained, while the common mode will preserve coherent (correlated) residual signal power from this source. Such information, however, is expected to be greatly suppressed since the station residuals result from a regression that already includes air pressure loading.

The reason why we estimate an admittance parameter of the predicted loading effect rather than applying the effect as a correction is as follows. The admittance coefficients that we obtain are systematically and significantly lower than unity. We suspect that the GPS orbits induce regional perturbations since atmospheric loading is not applied at the stage of orbit computation. Since only a small number of stations in northern Europe are used by the orbit centers, only a certain fraction of displacement is conveyed into the orbit.

A second issue is the possible mapping of air pressure related information into other

parameters of the GPS analysis. Here, the most probable candidate is the atmospheric delay parameter, and a particular reason to suspect it is the way the hydrostatic and the water vapor related delays are parameterized [Segall and Davis, 1996]. However, we can show that only submillimeter vertical site offsets can be expected when atmospheric pressure varies as much as  $\pm 30$  hPa.

Bottom pressure equilibrium requires days to weeks to establish in shallow waters. Since the Baltic Sea is a nearly enclosed basin, the inverse barometer response is certainly substantially delayed. Thus, it appears more promising to neglect the water response in the atmospheric loading model and add another signal channel in the linear regression representing the water level of the Baltic Sea at a tide gauge station nearby.

#### 4.4. Sea-Level Tilt

Data from the TOPEX satellite reveals a north-south sea-level tilt during the duration of the TOPEX experiment (1992–present). Since this timespan is nearly the same as that of the BIFROST data analyzed for this study, we might expect a secular site position variation as a result of the elastic loading associated with this tilt. In order to calculate this effect, we first used the TOPEX results from the Baltic to fit for north-south and east-west components of the sea-level tilt. (These results were provided by S. Nerem of the University of Texas at Austin.) Using the Kattegatt to define the boundary of the Baltic, we found that within the Baltic the observed TOPEX sea-level rates  $r(\lambda, \phi)$  at north latitude  $\lambda$  and east longitude  $\phi$  were well described by  $r(\lambda, \phi) = A + B(\lambda - \lambda_o) + C(\phi - \phi_o)$ , where  $\lambda_o = 18.237^\circ$ ,  $\phi_o = 57.979^\circ$ ,  $A = 7.7 \pm 0.2$  mm yr<sup>-1</sup>,  $B = -0.07 \pm 0.06$  mm yr<sup>-1</sup> per degree of longitude, and  $C = -1.4 \pm 0.1$  mm yr<sup>-1</sup> per degree of latitude. The uncertainties were determined by scaling the uncertainties determined using a unit-weighted least squares solution by the root-mean-square (RMS) residual rate of 4.8 mm yr<sup>-1</sup>. The distribution of the residuals was well described by a Gaussian distribution with the standard deviation equal to

the RMS residual; we did not, however, examine the residuals carefully for systematic geographic variations.

In the next step, we used the tilt results to obtain a Baltic-shaped load rate with a north-south variation of  $-1.4 \text{ mm yr}^{-1}$  per degree of latitude and no east-west tilt. We convolved this load with an elastic Green's function in a manner similar to that of the other loading calculations above to calculate vertical rates in  $1^\circ$  steps along a north-south profile along longitude  $20^\circ$ . As expected, the maximum vertical deformation occurred near the south of the Baltic, at latitude  $56^\circ$ , where we calculated a subsidence rate of  $\sim 0.25 \text{ mm yr}^{-1}$ .

Thus, although the sea-level "tilt" observed by TOPEX is quite large, the overall load produced by the Baltic Sea, which is rather small, is nearly negligible for our purposes. Furthermore, one would expect that such a tilt, if caused perhaps by wind stress, is quite variable over longer times, so that the effective secular elastic loading associated with this effect will on average decrease with time.

## 5. Error Analysis

In this section we carefully examine the possible influence of a number of errors on our main geophysical observable, the site velocities. We include this study for several reasons. The expected magnitude of GIA contribution to the velocities is fairly small, typically  $< 3 \text{ mm yr}^{-1}$  for the horizontal component and  $< 10 \text{ mm yr}^{-1}$  for the vertical. The technique of continuous GPS is rather new, and no careful analysis of errors has yet been performed for determinations of velocity obtained from these data. We begin by assessing the spatial and temporal dependence of variations observed in our position determinations.

## 5.1. Correlation Analysis

We anticipate that there may be a number of noise sources affecting the stations in a region in a similar way, such as satellite orbit errors, reference frame errors, errors at one or possibly more sites that are propagated through the network due to the type of network solution we perform, environmental conditions that change over a region in a coherent way (for example, soil surface reflectivity affected by climatic factors, snow covering antenna and radomes), and short-lived non-secular crustal deformations due to predominantly atmosphere and hydrosphere loading.

Since we have time series of perturbed site positions, we seek a method that takes advantage of the statistics inherent in the large amount of information and relate to the separation of local and regional signals and noises. We have chosen to represent the degree of correlation of perturbations to site position (eventually including coherent, transient motion) between stations using an Empirical Orthogonal Function (EOF) type of analysis. (*Davis and Elgered [1998]* used an EOF method with estimates of water vapor determined from BIFROST data.) We want to utilize this information in the adjustment when we solve for rates, offsets and other locally relevant parameters, thus attempting to discriminate between local deterministic processes and correlated transient signals.

Secular GIA motion is of course correlated between the sites. Thus we need a first stage where parameters for this process (and others we are aware of) are estimated and residuals formed, followed by a second stage where we then use these residuals to obtain improved values for the rate and other parameters.

In the locally relevant parameter set we include atmospheric loading since this perturbation can be predicted on a per-site basis. However, a certain fraction of atmospheric loading perturbations might actually be transferred into satellite orbit perturbations, since corrections of site positions due to this effect are not routinely estimated in the precise orbit generation phase. Thus, as we will see, the atmospheric

loading signal is attenuated in the GPS time series, although some signal apparently leaks in during the second (EOF) stage due to correlation between the common mode and the atmospheric loading time series.

**5.1.1. Procedure.** This section describes the two-stage least-squares procedure we have developed that uses the GPS time series of station positions to determine a combined set of parameters that include: (1) the usual set of rate and offset parameters; (2) admittance parameters for geophysical signals such as pressure and precipitation that we might expect to be correlated with the estimated GPS time series; and (3) between-site correlation parameters. We begin in the first step by looking for the solution to the linearized system

$$\mathbf{G} \cdot \mathbf{p} = \mathbf{d} + \boldsymbol{\epsilon} \quad (3)$$

The unknown parameter vector  $\mathbf{p}$  contains both the usual set of rate and offset parameters and the admittance parameters for geophysical signals for one station. The vector  $\mathbf{d}$  is a to-be-modeled time series (for example, north, east, or up components of position for one station) and  $\boldsymbol{\epsilon}$  its vector of errors. The matrix  $\mathbf{G}$  is the design matrix defined in the usual way. If we are including surface pressure in the model, then one of the columns of  $\mathbf{G}$  will be the surface pressure at the site corresponding to the epochs for which the determinations of  $\mathbf{d}$  were obtained.

As usual, the solution to (3) is obtained by minimizing the mean square residual and can usually be determined using the standard least-squares formulation. However, since this system can in general be underdetermined or otherwise singular, and for computational compatibility with the second step of the process, we solve (3) using the generalized inverse method of Lanczos [*Aki and Richards*, 1980]. In this method, we first normalize the system of equations (3) such that the expected variance of the  $\boldsymbol{\epsilon}$  is the unit matrix. (We assume for this analysis that the observations are uncorrelated.) We denote the normalized quantities with a tilde ( $\tilde{\mathbf{G}}$ ,  $\tilde{\mathbf{d}}$ , and so on). The generalized inverse of  $\tilde{\mathbf{G}}$  is expressed as a singular value decomposition (SVD), wherein we seek the solution

to the eigenvalue equations

$$\begin{pmatrix} \tilde{\mathbf{G}}^T \tilde{\mathbf{G}} \\ \tilde{\mathbf{G}} \tilde{\mathbf{G}}^T \end{pmatrix} \cdot \begin{pmatrix} \mathbf{u} \\ \mathbf{v} \end{pmatrix} = \lambda^2 \begin{pmatrix} \mathbf{u} \\ \mathbf{v} \end{pmatrix} \quad (4)$$

where  $\mathbf{u}$  is a matrix of eigenvectors that span the parameter space,  $\mathbf{v}$  is a matrix of eigenvectors that span the data space, and  $\lambda$  represents the set of eigenvalues. *Aki and Richards* [1980] demonstrate that  $\mathbf{u}$  and  $\mathbf{v}$  share the first  $m$  eigenvalues, where  $m$  is the minimum of the dimensions of  $\mathbf{u}$  and  $\mathbf{v}$ ; the remaining eigenvalues are zero.

In our analysis for this study, we modeled the time series of vertical components of station position for the BIFROST sites. In addition to rates and biases for each site, we estimated site-dependent sinusoidal amplitudes (in- and out-of-phase) with annual, semiannual, terannual, and quarterannual periods, and (site-dependent) admittance parameters for surface pressure.

In the second stage of the analysis the solution was repeated with the modification that for each site we also estimated parameters that represent admittance for the residuals calculated in the first stage for all the BIFROST sites. For example, if using the data from the Umeå site yields a non-zero admittance for the stage-one residuals from Kiruna site, that result indicates a correlation between the unmodeled signal from the first stage for Kiruna and the observed signal for Umeå. In this sense, the second stage is equivalent to a traditional (unweighted) EOF analysis. Moreover, in a manner analogous to a traditional EOF analysis, we keep only those parameters whose eigenvalues signify that they convey a significant amount of information.

In the second (EOF) stage, we define two subsets of the parameter space. The subset of the parameters that were estimated in the first stage we name  $\mathcal{C}$ ; these parameters will be estimated regardless of their eigenvalue. The subset consisting of the new (residual admittance) parameters of the EOF construct we name  $\mathcal{E}$ . Sorting the eigenvalues of  $\mathcal{E}$  by decreasing magnitude yields one which is the largest,  $\lambda_c$ . Associated with it is eigenvector  $\mathbf{v}_c$ , which is to be retained; the remaining subspace of  $\mathcal{E}$  is to be

ignored. In a traditional space-time EOF analysis  $\mathbf{v}_c$  is known as the first temporal eigenvector.

The eigenvector  $\mathbf{v}_c$  retained from subspace  $\mathcal{E}$  extends the data space to comprise a common mode. The common mode time-series is obtained from the parameter solution by simply projecting it on the subspace  $\mathcal{E}$  and inserting it into the model (3). The common mode construction is a form of a spatial filter performing a weighted mean, where the weights are devised by the eigenvalue process and hence by the data themselves. The procedure we devised may be contrasted to the filter of *Wdowinski et al.* [1997], which was formed by taking a mean of the time series for the stations in the network. Each observation is equally weighted regardless of uncertainty or station. In our procedure, we use the uncertainties and the station weights are determined by the station admittance parameters, calculated to minimize the mean-square residual.

As in a traditional EOF analysis, the relative signal power propagated through each eigenvector in the inverse solution is proportional to the squared magnitude of the eigenvalue. In our solutions using the vertical component of site position, the ratio  $\lambda_c^2 / \sum_j \lambda_j^2$  is typically on the order of 20%. The normalized  $\chi^2$  residual for the second stage is typically a factor of  $\sim 2$  smaller than that of the first stage, wherein no common-mode signal is estimated. In Figure 7 we show the normalized residuals for the first and second analysis stages along with the common mode signal.

**5.1.2. Spatial correlations.** The eigenvectors and eigenvalues carry information about the correlation of the time series among the sites, accounting for the model of the first adjustment stage. This information stems from the similarity of the scalar product used in the eigenvalue solution process and the manner in which correlations are computed. Figure 8, for example, contains a plot of the parameter eigenvectors for an analysis of a subset of 11 SWEPOS sites: Metsähovi, Skellefteå, Umeå, Sundsvall, Mårtsbo, Leksand, Sveg, Östersund, Vilhelmina, Arjeplog, and Kiruna. The 11 admittance parameters representing  $\mathcal{E}$  are the last 11 (parameter numbers 15–25). It is

clear from the primary eigenvector in Figure 8 that the contribution from the different sites is fairly large and constant. The exception might be the first site, Metsähovi. This site is used to constrain the reference frame (see above). The correlation between regional stations and a station which has been used for mapping into the reference frame is generally low because the average rotations and translations of the the small number of constraining stations that have been used are only slightly overdetermined; thus they are propagated throughout the network.

It is straightforward to show that the correlation coefficient  $\gamma_{jk}$  between time series from the  $j$ th and  $k$ th stations can be computed using the first spatial eigenvector of  $\mathcal{E}$ , denoted  $\mathbf{u}_c$ :

$$\gamma_{jk} = \lambda_c^2 u_{cj} u_{ck} / N \quad (5)$$

where  $N$  is the number of data. The expected low correlations with constraining stations, in this case Metsähovi (parameter #15), is clearly seen in Figure 9, which shows the correlation as a function of intersite distance. The remaining rate parameters exhibit great coherence ( $\gamma \simeq 0.5$ ) on a regional scale. Figure 9 does seem to indicate, however, that there is a clear but weak dependence of correlation on intersite separation. This result implies that the cause of the correlation is network-wide, indicating perhaps a reference frame or orbital-type effect.

**5.1.3. Effect of reference frame errors.** There are two types of reference frame errors to consider: errors formally accounted for by the error covariance matrix, and biases. In the ideal case of independent Gaussian measurement errors with perfect geodetic models, linear propagation of the measurement error covariance would yield an accurate characterization of the errors in geodetic model parameter estimates. Uncertainties in velocity estimates derived from such position determinations would similarly be accurate and well understood. In the real world, however, geodetic models are not perfect, measurement noise processes are not normally (i.e., Gaussian) distributed, and the measurement errors are not generally independent. Each of

these factors complicates the parameter estimation problem. The resulting parameter estimates are likely to be contaminated by systematic errors which are difficult, perhaps impossible, to fully assess.

An exhaustive list of the mechanisms through which systematic errors could manifest themselves as reference frame biases and their respective importance will require continued research. However, it is not difficult to list some important potential mechanisms. Deficiencies in the geodetic models describing satellite orbital dynamics or the dynamics of Earth's orientation, for example, have obvious implications for an accurate reference frame realization. For local networks, errors in the atmospheric modeling or other spatially correlated errors, such as those due to similar scattering at similar monuments, could result in local reference frame biases. The same is also true of over-constrained a priori parameter estimates, such as for satellite ephemerides, satellite clock variations, or site positions, particularly if these a priori estimates were themselves correlated. These "fiducial errors" have been appreciated for some time [e.g., *Larson and Agnew*, 1991]. Site specific errors, associated with such phenomena as multipath or antenna phase center variations, may manifest themselves indirectly as reference frame biases as we now discuss.

Trade-offs between parameters of the geodetic model, such as between the implicit specifications of the satellite and GPS network orientations, render the site position determination problem ill-posed. That is, in the absence of additional constraints, the matrix of partial derivatives relating the basic prefit GPS carrier phase and pseudo range residuals (i.e., the data) to the first order corrections to the a priori parameter estimates (including site positions, satellite parameters, and Earth orientation parameters) is singular. The degree of singularity depends on the geometry of the tracking network; regional scale networks are "less singular" than global scale networks. A priori information, such as knowledge of the positions of certain sites in the network, is often effectively employed to regularize this singularity. The resulting position estimates

implicitly define a reference frame. Depending on the level of constraints imposed and assuming, for now, that this level is consistent with the true errors in the a priori estimates, some linear combinations of the model parameter estimates, such as the differences in positions of the sites, may be significantly better determined than the “absolute” model parameters themselves. However, site specific errors not formally accounted for by the covariance matrix will affect all components of the vector of linear combinations involving the contaminated site. The importance of any reference frame errors resulting from this transformation will thus depend on the transformation itself (the particular linear combination), the number of sites suffering from systematic errors, and the size of these systematic errors.

## 5.2. Power Spectral Analysis

The time series contains signals that are not well modeled by simple rate and offset terms. To assess these errors it is most useful to examine their power spectrum. Generally, one computes a set of postfit residuals, then uses the residuals as input to, for instance, an FFT algorithm. Windowing or filtering may be performed at some point. In almost all cases the algorithm for computing the power spectrum assumes that the data are equally spaced and equally weighted. Given the nature of our data, neither of these assumptions is very good. Moreover, it would be useful to be able to assess the effects of data gaps and the estimation of model parameters, especially rate and offset parameters, on the estimated power spectrum.

We have implemented a method for estimating a limited set of components for the power spectrum of the unmodeled signals in our time series. In this method, we estimate a series of coefficients to sinusoidal terms simultaneously with the rate and offset parameters. In effect, we used a very truncated form of this when we estimated coefficients to annual sinusoids (see above). The following discussion will apply to data from sites with long time series only, the SWEPOS sites and Metsähovi.

Given the total timespan of four years for these series of daily estimates, an FFT-type algorithm would estimate spectral components for frequencies  $k\Delta f_{min}$ ,  $k = 1, \dots, \frac{N}{2}$ , where  $\Delta f_{min} = 0.25$  cycles per year (cpy) and  $N \simeq 1460$ . It is the lowest-frequency components that are of most interest, since the presence of power at these frequencies might indicate errors having correlation times long enough to significantly influence our rate estimates. However, because we are estimating a rate parameter and offset parameters that can absorb power at these lower frequencies, we might expect that solutions containing low-frequency power-spectrum terms might be fairly unstable. In fact, we see exactly this result. Although it depends on the specific site, in general we cannot resolve well the power-spectrum parameters for frequencies lower than about 1 cpy.

We have therefore included spectral components for frequencies  $k\Delta f_{min}$  with  $\Delta f_{min} = 1$  cpy and  $1 \leq k \leq 64$ . Above this maximum frequency, the spectral components are generally not significant. Examples of the power spectra are shown in Figure 10. The spectra tend to be reddened, especially those for the vertical component of site position. The spectra for the vertical components are greater in magnitude than those for the horizontal components, as might be expected. The spectra for the horizontal components tend to be flatter. The north component especially tends to have (theoretically) significant peaks at higher frequencies.

The spectra we have calculated indicate that there is a great deal of low-frequency power in the variations of site position that is not properly modeled as a secular variation with offsets. The source of these variations cannot be determined from the power spectra alone. Spectra of residuals from our EOF analyses (not shown) indicate that some of the power is associated with network-wide effects. Some, but not all, of the power is therefore associated with site or region-wide sources of error. For example, we know that the snow effects (see below) cause errors with pseudo-annual periods. From our analysis of monument stability (see below), it seems unlikely that a large component

of the power is associated with highly localized monument motions.

Visual inspection of the power spectra lead us to conclude that the spectral indices for these spectra are in the range of  $-1$  to  $-2$ , consistent with the analyses of *Zhang et al.* [1997] for GPS sites in southern California and *Mao et al.* [1999] for global sites. Again, the horizontal components tend to be a little flatter, with spectral indices closer to  $-1$ . As pointed out by these authors and others, if these spectral components are representative of a stochastic noise process with a long correlation time, then the standard errors one determines for the slopes are significantly underestimated. However, it is probable, as we have pointed out, that our error spectra contain some truly periodic terms. Indeed, many of the spectra shown by *Mao et al.* [1999] have peaks near annual frequencies. It is clear, though, from our attempts to estimate spectral components with frequencies lower than 1 cpy, that noise at these lower frequencies would significantly effect our estimates of the rates. Further studies regarding the detailed spectral composition of our time series will be possible when we have longer timespans of determinations with no changes in equipment.

### 5.3. Atmosphere

As discussed in Section 3, the GIPSY analysis software uses a stochastic filter to model the temporal variability of the zenith atmospheric propagation delay. The a priori model for the propagation delay for each site consists of a constant ellipsoidal-height-dependent term representing the hydrostatic zenith delay [*Davis et al.*, 1985] that is “mapped” to the elevation angle of the GPS signal using the Lanyi dry mapping function [*Lanyi*, 1984]. The a priori wet zenith delay is taken to be 100 mm. Corrections to this a priori total zenith delay are estimated by adopting that the Lanyi wet mapping function to describe how the correction maps with elevation angle. In effect, this procedure maps the combined corrections to both the hydrostatic and the wet zenith delays using the wet mapping function. Using a simulation procedure similar

to that of *Elósegui et al.* [1995], we find that the error in the vertical component of site position (the primary geodetic parameter affected) caused by mapping the correction to the hydrostatic zenith delay using a wet mapping function is less than  $\pm 2$  mm, assuming an annual pressure variation of  $\pm 30$  mbar.

The mapping functions used assume that the atmosphere is azimuthally symmetric as viewed from the station. Horizontal structure in the atmosphere nevertheless generally leads to an effective azimuth-dependent mapping function. In particular, horizontal gradients in the refractive index lead to sinusoidal variations in azimuth [e.g., *Davis et al.*, 1993]. We have not incorporated this model into our phase model or estimated any parameters associated with horizontal structure, leaving this to future studies. Although such errors can be quite large at low elevation angles [*Davis et al.*, 1993], we do not expect this error to bias systematically the estimate of the site rates. Of much greater concern are the azimuthal-dependent effects of snow accumulation on the radomes.

#### 5.4. Signal Effects

In the course of our experiment we have investigated several errors involving the propagation of the GPS signals in the nearby environment of the GPS antenna. Near-field scattering [*Elósegui et al.*, 1995] involves the reflection of the GPS signal off surfaces close to the GPS antenna. This effect is different from multipath in that the reflecting surfaces are well within the near-field of the antenna. These surfaces thus become electromagnetically coupled to the antenna, effectively creating a new antenna. One such reflecting surface is the pillar directly beneath the GPS antenna, which often (and in the case of our Swedish sites) has a metal plate embedded onto its top surface. *Jaldehyag et al.* [1996b] investigated this effect for sites of our Swedish GPS network, and found that for the most part the scattering effects are equal for all the sites (and therefore cancel in the baselines), since with the exception of the Onsala GPS site all

the pillars are identical and the local vertical direction at each of the sites is nearly parallel. It is possible that this effect is in part responsible for the common-mode site variations we find (Section 5.1). In the principal component analysis we performed, we found that the component of the spatial eigenvector for the Onsala site had the smallest value of all the Swedish sites.

The error associated with the signal scattering effect is quite large, even when the size of the phase error is small. In the least-squares estimation procedure, the errors in each of these parameters can be “magnified” and yet the summed contribution to the phase can be fairly small. The effect on the horizontal components is smaller than that for the vertical but not zero. *Elósegui et al.* [1995] found that the error in the estimated vertical component was therefore dependent on the geometrical distribution of observations on the sky. For a given fixed constellation and sequence of observations, the error in the estimate of site position is dependent on the minimum elevation angle accepted for use in the data analysis. In practice, however, it is not possible to maintain a fixed geometrical distribution of observations on the sky, due to data dropouts.

We found also that snow and ice, which adheres to the radome and accumulates, is a significant source of error, simply by causing an additional propagation delay. This effect was first noted by *Webb et al.* [1995] when several meters of snow buried a GPS antenna near Long Valley. The amount of snow and ice which accumulates on our antennas is much smaller, perhaps several decimeters maximum, and the problem is therefore more insidious. (The lower amount of snow also tends to be distributed unevenly on the radome.) *Jaldehyag et al.* [1996a] found that they were able to approximate the results from elevation angle cutoff tests using a conically symmetric distribution of snow, but visual inspection of our sites indicates that real conditions are not so ideal.

A final effect which we have already mentioned is the propagation delay due to the radome. In theory an expression can be developed for this contribution and in the future we plan to test such a model. For this paper, however, we have simply introduced

an offset to the time series on the epochs which we have changes radomes.

### 5.5. Monument Stability

As described in the section describing the GPS networks, we monitor the relative position of the pillar reference point within a local (10–15 m area) network of reference pins. The determination of the pillar position is given in Table 4. The expected uncertainty of these determinations, based on propagation of the instrumental errors through the resection technique, is  $\sim 0.1$  mm. Based on the RMS analysis of all the data, the standard deviation of a single measurement is 0.2 mm for the north, 0.3 mm for the east, and 0.4 mm for the vertical. However, there are several occasions when repeated measurements are obtained in a single day. The five repeated measurements from the Leksand site, for instance, yield RMS differences of 0.01 mm for north, 0.04 for east, and 0.06 mm for vertical. The single repeated measurement for Kiruna, on the other hand, yields an RMS difference (based on two measurements) of 0.2 (north), 0.3 (east), and 0.1 mm (up), roughly consistent with the same statistics for the single repeated measurement for the Överkalix site: 0.03 (north), 0.1 (east), and 0.1 mm (up); and for the Norrköping site: 0.1 (north), 0.1 (east), and 0.1 mm (up). If we combine the Kiruna, Överkalix, and Norrköping repeat measurements, we find an RMS error of 0.10 (north), 0.18 (east), and 0.10 (north). We will therefore adopt the average 0.13 mm as our uncertainty in each of the components. We have no explanation as to why the differences in the repeated Leksand measurements are so small relative to these values. Eliminating the multiple measurements by replacing them with their average, the overall RMS variations for all sites are 0.20 (north), 0.31 (east), and 0.38 mm (up). Thus, overall, the average RMS variations are consistent with the adopted measurement error at the level of  $3\sigma$ .

Nevertheless, for individual pillars, most notably Skellefteå S (east component) and Umeå (up component), the variations are greater than 1 mm. In the case of

Skellefteå S, the variation for the north and vertical component are small, so unless the pillar happened to have moved on a nearly north-south axis this result is spurious. The Umeå variation is in the vertical component, which, one can surmise, could experience motions independent from the horizontal components. The most worrisome effect would be settling of the pillar. However, the measurements indicate that the pillar was 2.3 mm higher relative to the nearby network in June 1995 than in June 1993. In order to resolve this and other issues, further pillar measurements are planned for the near future. However, these future measurements will be obtained in a slightly different manner. Reflectors will be fixed to the pillars and the antenna will not have to be removed.

More frequent measurements were obtained on the Leksand site than for others, for test purposes. The time series of measurements is shown in Figure 11. *Langbein and Johnson* [1997] have investigated temporal variations in line lengths determined from EDM; their analysis indicates that the PSD of the variations follows a  $f^{-2}$  behavior, indicative of a random walk process. They argue that these variations are associated with pillar motions. Although our Leksand data are sparse, we can perform a maximum-likelihood analysis on the assumption that the temporal variations of the pillar position can be described by a random walk, and that the measurement uncertainties are 0.13 mm, as described above. For the three components, the maximum likelihood estimate of the random walk variance was 0.3 (north), 0.2 (east), and 0.1 mm<sup>2</sup> yr<sup>-1</sup> (up), values much less than the average value of 1.7 mm<sup>2</sup> yr<sup>-1</sup> found by *Langbein and Johnson* [1997]. The monuments investigated by these authors are very similar to those we used for the Swedish GPS network: for instance, the sites of the Parkfield network used galvanized steel pipe of diameter 20 mm placed into augered holes 2 m deep. Near two of these Parkfield sites, special monuments were installed to a depth of 10 m; the average random walk variance for these two deep anchored monuments was  $\sim 2$  mm<sup>2</sup> yr<sup>-1</sup>, whereas that for the shallow monuments was  $\sim 15$  mm<sup>2</sup> yr<sup>-1</sup> [*Langbein and Johnson*, 1997].

The average random walk variances, based on the difference between end-point measurements for the 20 sites with pillar measurements spanning more than six months, is 0.08 (north), 0.21 (east), and 0.26 mm<sup>2</sup> yr<sup>-1</sup> (up).

## 6. Discussion and Future Work

We have used a regional continuous GPS network to measure three-dimensional crustal deformation rates in Fennoscandia. The observed rates correlate highly to rates predicted for a viscoelastic Earth undergoing present-day glacial isostatic adjustment (GIA) due to the rapid melting of Late Pleistocene glaciers. The observed rates correlate well also with observed sea-level rates obtained from tide-gauge data over the last 30 years.

We see no evidence for the regional shear inferred by *Pan and Sjöberg* [1999] using a much smaller GPS network and only two campaign measurements. *Pan and Sjöberg* [1999] found relative horizontal motions across the north-south extension of the Baltic Sea to be 2–3 mm yr<sup>-1</sup>, whereas using the Table 2 rates we find the motions of these sites to be generally less than 1 mm yr<sup>-1</sup>, probably within the uncertainties. Our velocities are roughly consistent with the expected velocities near the center of uplift.

We get much better agreement with theoretical predictions of crustal velocity based on GIA, relative to the “standard errors,” in the radial (vertical) component than in the horizontal components of station velocity. This results may seem counterintuitive since radial velocity estimates obtained from GPS data are well known to be less accurate than horizontal velocity estimates. Nevertheless, there could be several explanations for this situation. The standard errors for the vertical component could be more realistic, since they are by nature larger. If, for example, there were some systematic error (correlated in time or not) that was about equal in its effects on the three components of site position, then proportional to the standard error the systematic error would be much larger in the horizontal components. Errors in the ice model would also tend to have a

proportionally greater effect on the horizontal components of velocity. For example, a slightly misplaced maximum ice thickness could easily change the predicted horizontal rates by 100% near the maximum, while changing the radial rate by only  $\sim 10\%$ .

Although we have much evidence for time-correlated behavior in the site-position time series both from power spectrum calculations and from visual inspection of the time series themselves, our measurements for pillar motion indicate that the top of the pillar moves less than 1 mm relative to a very local network of pins. This result may indicate that “monument instability,” if it exists for our sites, may not be the result of local deformation of the crust. If so, then the “footprint” would have to be extended in order to measure this phenomenon.

The empirical orthogonal function (EOF) analysis we performed revealed a correlated noise in radial position time series across a large region ( $\sim 1000$  km). This analysis also indicated that these correlations decrease slightly with distance. Typical RMS residuals for our radial time series are 7 mm. The EOF analysis indicated that over half of the noise contributing to the RMS residual is from this correlated noise. The source of the correlated noise, unfortunately, cannot be revealed by an EOF analysis. We and others have speculated that the correlations are due to systematic errors in the satellite orbits, terrestrial reference frame, or both. If the source of this error can be identified and eliminated, then there is the possibility of reducing velocity uncertainties from GPS by  $\sim 50\%$ .

In the near future, we will also extend our analysis to include more recent data. It is clear from our analysis that the several changes we have made to the GPS equipment have limited the achievable accuracy. Longer time series with no equipment changes should provide more reliable rate estimates.

We have not attempted to determine our “true” uncertainties. We have reported the “standard errors” so that users of the rates may have the straightforward results of the least-squares analysis. The standard errors may be scaled or otherwise increased as

required. Based on a linear fit to the predictions we presented in the paper, the standard errors would have to be increased a factor of  $\sim 8$  for the horizontal components and a factor of  $\sim 3$  for the vertical to achieve  $\chi^2$  values of unity. These are much larger than the scale factors found in Section 3.3. The comparison to the model assumes, however, that all the disagreement between the observed and predicted rates is caused by errors in the observed rates. In a future work, we will use the difference between the observed and predicted rates to infer errors in the the Earth and ice models used to obtain the predictions. The degree of fit can then be used to asses much better the errors in the observed rates.

The results presented here provide the first dense regional geodetic determinations of ongoing crustal deformation associated with GIA. The rates estimated herein are intended to be used as a new observable in the study of this phenomenon. We will also use the radial rates to correct tide-gauge data for vertical crustal motion to obtain absolute sea-level rates.

**Acknowledgments.** This work was supported by NASA grants NAG5-1930 and NAG5-6068, NSF grant EAR-9526885, the National Science and Engineering Research Council of Canada, the Swedish Natural Science Research Council, the Swedish Council for Planning and Coordination of Research (FRN), the Knuth and Alice Wallenberg Foundation, Posiva Oy of Finland, and the Smithsonian Institution. GPS data in non-continuous mode were obtained with the support of the University Navstar Consortium (UNAVCO) Facility. We thank S. Nerem for providing Baltic sea-level rates estimated from his analysis of TOPEX data. We greatly appreciate the comments and suggestions of M. Ekman. In the analysis, data from sites of the IGS was used. These data were obtained from the NASA Crustal Dynamics Data Information System (CDDIS) and University of California at San Diego SOPAC archives. Some figures were generated using Generic Mapping Tools (GMT) version 3 [*Wessel and Smith, 1995*].

## References

- Aki, K. and Richards, P. G., *Quantitative Seismology, Theory and Methods*, Vol. 2, Freeman, San Francisco, 1980.
- BIFROST Project, GPS measurements to constrain geodynamic processes in Fennoscandia, *Eos Trans. AGU*, 77, p. 337 & 341, 1996.
- Blewitt, G., Advances in Global Positioning System technology for geodynamics investigations: 1978–1992, in *Contributions of space geodesy to geodynamics: Technology*, edited by D. E. Smith and D. L. Turcotte, Geodynamics Series, Vol. 25, American Geophysical Union, Washington, D.C., 195–213, 1993.
- Broeker, W. S., and J. van Donk, Insolation changes in ice volumes and the  $\delta^{18}\text{O}$  record in deep-sea cores, *Rev. Geophys. Space Phys.*, 8, 169–198, 1971.
- Chappell, J., and N. J. Shackleton, Oxygen isotopes and sea level, *Nature*, 324, 137–140, 1986.
- Chen, R., and J. Kakkuri, Feasibility study and technical proposal for long-term observations of bedrock stability with GPS, *Rep. YJT-02*, Nuclear Waste Comm. Finn. Power Companies, Helsinki, 1994.
- Davis, A., A. Marshak, W. Wiscombe, and R. Cahalan, Multifractal characterizations of nonstationarity and intermittency in geophysical fields: Observed, retrieved, or simulated, *J. Geophys. Res.*, 99, 8055–8072, 1994.
- Davis, J. L., and G. Elgered, The spatio-temporal structure of GPS water-vapor determinations, *Phys. Chem. Earth*, 23, 91–96, 1998.
- Davis, J. L., T. A. Herring, I. I. Shapiro, A. E. E. Rogers, and G. Elgered, Geodesy by radio interferometry: Effects of atmospheric errors on estimates of baseline length, *Radio Science*, 20, 1593–1607, 1985.
- Davis, J. L., G. Elgered, A. E. Niell, C. E. Kuehn, Ground-based measurements of gradients in the “wet” radio refractivity of air, *Radio Science*, 28, 1003–1018, 1993.
- Davis, J. L., J. X. Mitrovica, H.-G. Scherneck, and H. Fan, Investigations of Fennoscandian glacial isostatic adjustment using modern sea-level records, *J. Geophys. Res.*, 104, 2733–2747, 1999.

- Denton, G. H., and I. J. Hughes (Eds.), *The Last Great Ice Sheets*, John Wiley, New York, 1981.
- Dziewonski, A. M. and D. L. Anderson, Preliminary reference Earth model (PREM), *Phys. Earth. Planet. Inter.*, 25, 297–356, 1981.
- Elósegui, P., J. L. Davis, R. T. K. Jaldehag, J. M. Johansson, A. E. Niell, and I. I. Shapiro, Geodesy using the Global Positioning System: The effects of signal scattering on estimates of site position, *J. Geophys. Res.*, 100, 9921–9934, 1995.
- Emardson, T. R., J. M. Johansson, and G. Elgered, The systematic behavior of water vapor estimates using four years of GPS observations, *Trans. IEEE Geosci. Remote Sensing*, GE-38, 324–329, 2000.
- Farrell, W. E. and J. A. Clark, On postglacial sea level, *Geophys. J. R. Astron. Soc.*, 46, 647–667, 1976.
- Fjeldskaar, W., Viscosity and thickness of the asthenosphere detected from the Fennoscandian uplift, *Earth and Planet. Sci Lett.*, 126, 399–410, 1994.
- Haskell, N. A., The motion of a fluid under a surface load, 1, *Physics*, 6, 265–269, 1935.
- Heflin, M., W. Bertiger, G. Blewitt, A. Freedman, K. Hurst, S. Lichten, U. Lindqwister, Y. Vigue, F. Webb, T. Yunck and J. Zumberge, Global geodesy using GPS without fiducials, *Geophys. Res. Lett.*, 19, 131–134, 1992.
- Jaldehag, R. T. K., J. M. Johansson, P. Elósegui, J. L. Davis, Geodesy using the Swedish permanent GPS network: Effects of snow accumulation on estimates of site positions, *Geophys. Res. Lett.*, 23, 1601–1604, 1996a.
- Jaldehag, R. T. K., J. M. Johansson, B. O. Rönnäng, P. Elósegui, J. L. Davis, and I. I. Shapiro, Geodesy using the Swedish permanent GPS network: Effects of signal scattering on estimates of relative site positions, *J. Geophys. Res.*, 101, 17,841–17,860, 1996b.
- James, T. S., and A. Lambert, A comparison of VLBI data with the ICE-3G glacial rebound model, *Geophys. Res. Lett.*, 20, 871–874, 1993.
- Koivula, H., M. Ollikainen and M. Poutanen, Use of the Finnish Permanent GPS network (FinnNet) in regional GPS Campaigns, *Proc. IAG General Assembly*, 1997.
- Koivula, H., M. Ollikainen and M. Poutanen, The Finnish Permanent GPS Network, *Proc. Gen. Assembly Nordic Geodetic Commission*, Gävle, Sweden, 1998.

- Lambeck K., C. Smither and P. Johnston, Sea-level change, glacial rebound and mantle viscosity for northern Europe, *Geophys. J. Int.*, *134*, 102–144, 1998a.
- Lambeck K., C. Smither and M. Ekman, Tests of glacial rebound models for Fennoscandinavia based on instrumented sea- and lake-level records, *Geophys. J. Int.*, *135*, 375–387, 1998b.
- Langbein, J., and H. Johnson, Correlated errors in geodetic time series: Implications for time-dependent deformation, *J. Geophys. Res.*, *102*, 591–564, 1997.
- Lanyi, G. E., Tropospheric Delay Effects in Radio Interferometry, *TDA Progress Rep. 42-78*, Jet Propulsion Lab., Pasadena, California, 152–159, 1984.
- Larson, K. M., and D. C. Agnew, Application of the Global Positioning System to crustal deformation measurement, 1. Precision and accuracy, *J. Geophys. Res.*, *96*, 16,547–16,565, 1991.
- Le Provost, C., M. L. Genco, F. Lyard, P. Vincent, and P. Canceil, Spectroscopy of the world ocean tides from a finite element hydrodynamical model, *J. Geophys. Res.*, *99*, 24,777–24,798, 1994.
- Mao, A., C. G. A. Harrison, and T. H. Dixon, Noise in GPS coordinate time series, *J. Geophys. Res.*, *104*, 2797–2816, 1999.
- McCarthy, D. (ed.), IERS (1996) Standards, *IERS Tech. Note 21*, Observatoire de Paris, 1996.
- McConnell, R. K., Viscosity of the mantle from relaxation time spectra of isostatic adjustment, *J. Geophys. Res.*, *73*, 7089–7105, 1968.
- Milne, G. A., *Refining Models of the Glacial Isostatic Adjustment Process*, Ph.D. Thesis, Dept. of Physics, University of Toronto, 126 pp., 1998.
- Milne, G. A. and J. X. Mitrovica, Postglacial sea-level change on a rotating earth, *Geophys. J. Int.*, *133*, 1–19, 1998.
- Mitrovica, J. X., G. A. Milne, and J. L. Davis, The influence of glaciation-induced perturbations in the Earth's rotation on present day 3-D crustal deformations, *Geophys. J. Int.*, submitted, 2000.
- Mitrovica, J. X., Haskell [1935] revisited, *J. Geophys. Res.*, *101*, 555–569, 1996.
- Mitrovica, J. X. and W. R. Peltier, The inference of mantle viscosity from an inversion of the Fennoscandian relaxation spectrum, *Geophys. J. Int.*, *114*, 45–62, 1993.

- Mitrovica, J. X., J. L. Davis, and I. I. Shapiro, Constraining proposed combinations of ice history and Earth rheology using VLBI-determined baseline length rates in North America, *Geophys. Res. Lett.*, *20*, 2387–2390, 1993.
- Mitrovica, J. X., J. L. Davis and I. I. Shapiro, A spectral formalism for computing three-dimensional deformations due to surface loads, 1, Theory, *J. Geophys. Res.*, *99*, 7075–7101, 1994a.
- Mitrovica, J. X., J. L. Davis, and I. I. Shapiro, A spectral formalism for computing three-dimensional deformations due to surface loads, 2, Present-day glacial isostatic adjustment, *J. Geophys. Res.*, *99*, 7075–7102, 1994b.
- Pan, M., and L. E. Sjöberg, Estimating present-day postglacial rebound and horizontal movements in Fennoscandia by repeated GPS campaigns in 1993 and 1997, *Geophys. Res. Lett.*, *26*, 771–774, 1999.
- Paunonen, M., Height stabilised 20-metre antenna mounting system of the CIGNET GPS station at Metsähovi, *Newsletter of Space Geodetic Measurements Sites Subcommission (SGMS)*, IAG, IUGG, International Coordination of Space Techniques for Geodesy and Geodynamics (CSTG), Vol. 4, No. 1, pp. 7–10, 1993.
- Pugh, D. T., N. E. Spencer, and P. L. Woodworth, *Data Holdings of the Permanent Service for Mean Sea Level*, 156 pp., Permanent Serv. for Mean Sea Level, Bidston, Birkenhead, England, 1987.
- Segall, P., and J. L. Davis, GPS applications for geodynamics and earthquake studies, *Annu. Rev. Earth planet. Sci.*, *25*, 301–336, 1997.
- Scherneck, H.-G., A parametrized solid earth tide model and ocean tide loading effects for global geodetic baseline measurements, *Geophys. J. Int.*, *106*, 677–694, 1991.
- Schupler, B. R., R. L. Allshouse, and T. A. Clark, Signal characteristics of GPS user antennas, *Navigation*, *41*, 277–295, 1994.
- Schönwiese, C.-D., and J. Rapp, *Climate Trend Atlas of Europe Based on Observations 1891–1990*, 228 pp., Kluwer, Boston, 1997.
- Sillard, P., Z. Altamimi, and C. Boucher, The ITRF96 realization and its associated velocity field. *Geophys. Res. Lett.*, *25*, 3223–3226, 1998.

- Spilker, J. J., GPS signal structure and theoretical performance, in *Global Positioning System: Theory and Applications, Volume I*, edited by B. W. Parkinson and J. J. Spilker Jr., 793 pp., AIAA, Washington, DC., 1996.
- Tushingham, A. M. and W. R. Peltier, ICE-3G: A new global model of late Pleistocene deglaciation based upon geophysical predictions of postglacial relative sea level change, *J. Geophys. Res.*, *96*, 4497–4523, 1991.
- vanDam, T. M., and J. Wahr, The atmospheric load response of the ocean determined using Geosat altimeter data, *Geophys. J. Int.*, *113*, 1–16, 1993.
- Vening Meinesz, F. A., The determination of the Earth's plasticity from the postglacial uplift of Scandinavia: isostatic adjustment, *Kon. Akad. Wetensch.*, *40*, 654–662, 1937.
- Wdowinski, S., Bock, Y., Zhang, J., Fang, P., and Genrich, J., Southern California Permanent Geodetic Array: Spatial filtering of daily positions for estimating coseismic and postseismic displacements induced by the 1992 Landers earthquake, *J. Geophys. Res.*, *102*, 18,057–18,070, 1997.
- Webb, F. H. and J. F. Zumberge, An Introduction to the GIPSY/OASIS-II, *JPL Publication*, Jet Propulsion Laboratory, Pasadena, CA, 1993.
- Webb, F. H., M. Bursik, T. Dixon, F. Farina, G. Marshall, and R. S. Stein, Inflation of Long Valley Caldera from one year of continuous GPS observations, *Geophys. Res. Lett.*, *22*, 195–198, 1995.
- Wessel, P., and W. H. F. Smith, New version of the Generic Mapping Tools released, *Eos Trans. AGU*, *76*, 329, 1995.
- Wieczerkowski, K., J. X. Mitrovica and D. Wolf, A revised relaxation-time spectrum for Fennoscandia, *Geophys. J. Int.*, *139*, 69–86, 1999.
- Wolf, D., An upper bound on lithosphere thickness from glacio-isostatic adjustment in Fennoscandia, *J. Geophys.*, *61*, 141–149, 1987.
- Wolf, D., Note on estimates of the glacial-isostatic decay spectrum for Fennoscandia *Geophys. J. Int.*, *127*, 801–805, 1996.
- Wübbler, Ch. and W. Krauss, The two-dimensional seiches of the Baltic Sea, *Oceanol. Acta*, *2*, 435–446, 1979.

Zhang, J., Y. Bock, H. Johnson, P. Feng, S. Williams, J. Genrich, S. Wdowinski, and J. Behr, Southern California Permanent GPS Geodetic Array: Error analysis of daily position estimates and site velocities, *J. Geophys Res.*, *102*, 18,035–18,055, 1997.

---

G. Elgered, J. M. Johansson, B. O. Rönnäng, H.-G. Scherneck, Onsala Space Observatory, Chalmers University of Technology, S-439 92 Onsala, Sweden. (e-mail: kge@oso.chalmers.se; jmj@oso.chalmers.se; bor@oso.chalmers.se; hgs@oso.chalmers.se)

R. A. Bennett, J. L. Davis, P. Elósegui, G. A. Milne, I. I. Shapiro, Harvard-Smithsonian Center for Astrophysics, 60 Garden Street, Cambridge, MA 02138. (e-mail: rbennett@cfa.harvard.edu; jdavis@cfa.harvard.edu; pelosegui@cfa.harvard.edu; gmilne@cfa.harvard.edu; ishapiro@cfa.harvard.edu)

J. X. Mitrovica, Department of Physics, University of Toronto, 60 St. George St., Toronto, Ontario M5S 1A7, Canada. (e-mail: jxm@physics.utoronto.ca)

H. Koivula, M. Poutanen, M. Vermeer, Finnish Geodetic Institute, Geodeetinrinne 2, FIN-02430 Masala, Finland. (e-mail: Hannu.Koivula@fgi.fi, Markku.Poutanen@fgi.fi; Martin.Vermeer@fgi.fi)

B. Jonsson, Division of Geodetic Research, National Land Survey, S-801 82 Gävle, Sweden. (e-mail: martine@lmv.lm.se)

Received ; revised ; accepted .

---

<sup>1</sup>Onsala Space Observatory, Chalmers University of Technology, Onsala, Sweden.

<sup>2</sup>Harvard-Smithsonian Center for Astrophysics, Cambridge, Massachusetts.

<sup>3</sup>Now at Dept. of Geological Sciences, University of Durham, Durham, England.

<sup>4</sup>Finnish Geodetic Institute, Masala, Finland.

<sup>5</sup>Department of Physics, University of Toronto, Toronto, Canada.

<sup>6</sup>Division of Geodetic Research, National Land Survey, Gävle, Sweden.

Table 1. BIFROST site histories.

Site	IERS Domes No. <sup>b</sup>	Net-work <sup>c</sup>	Installed/Modified	Receiver <sup>d</sup>	Antenna <sup>e</sup>	Ra-dome <sup>f</sup>	Monument <sup>g</sup>	Approximate Position <sup>a</sup>			
								North Latitude	East Longitude	Height, m	
Arjeplog		S	93/08/20	8000	DM T	Delft	SWEPOS	66° 19'	18° 07'	489.2	
			95/02/03			Type A					
			95/08/01	Z-XII							
			96/06/28			None					
			96/10/29			Type B					
Borås		S	96/11/12	Z-XII	DM T	Ash	SWEPOS	57° 43'	12° 53'	220.0	
Hässleholm		S	93/08/20	8000	DM T	Delft	SWEPOS	56° 06'	13° 43'	114.1	
			95/05/19		*						
			95/06/10			Type A					
			95/08/01	Z-XII							
			96/07/01			None					
			96/11/12			Type B					
Joensuu	10512M001	F	95/06/15	Z-XII	DM Ash	Ash	2.5 m SG	62° 23'	30° 06'	113.7	
Jönköping		S	93/08/20	8000	DM T	Delft	SWEPOS B	57° 45'	14° 04'	260.4	
			94/06/23		*						
			95/06/24			Type A					
			95/05/21		*						
			95/08/01	Z-XII							
			96/07/03			None					
			96/11/10			Type B					
Karlstad		S	93/08/20	8000	DM T	Delft	SWEPOS	59° 27'	13° 30'	114.3	
			95/02/08			Type A					
			95/05/23		*						
			95/08/01	Z-XII							
			96/07/03			None					
			96/11/15			Type B					
Kevo		F	96/07/05	Z-XII	DM Ash	Ash	5 m SG	69° 45'	27° 00'	135.9	
Kiruna		S	93/08/01	8000	DM T	Delft	SWEPOS	67° 53'	21° 04'	498.0	
			93/08/17		*						
			94/06/15		*						
			95/06/16		*						
			95/07/10			Type A					
			95/08/01	Z-XII							
			96/07/30			None					
			96/10/30			Type B					
Kivetty		F	96/03/05	Z-XII	DM Ash	Ash	2 m CP	62° 49'	25° 42'	216.3	
Kuusamo		F	96/10/30	Z-XII	DM Ash	Ash	2.5 m SG	65° 55'	29° 02'	379.0	
Leksand		S	93/08/01	8000	DM T	Delft	SWEPOS	60° 43'	14° 53'	478.1	
			93/08/11		*						
			94/01/18		*						
			94/02/06		*						
			94/03/08		*						
			94/04/15		*						
			94/06/14		*						
			94/08/25		*						
			95/01/30			Type A					
			95/08/01	Z-XII							
			95/10/05		*						
			96/06/27			None					
			96/10/25			Type B					
Lovö		S	93/08/01	8000	DM Ash	Delft	SWEPOS C	59° 20'	17° 50'	79.7	
			93/10/28		*						
			95/05/16			Type A					

			95/06/15		*						
			95/08/01	Z-XII							
			96/06/28								
			96/11/07								
Metsähovi	10503S011	F	92/01/01	SNR-C	DM B	None	25 m SG IS	60° 13'	24° 24'	94.6	
			95/04/30	8100							
Mårtsbo		S	93/08/01	8000	DM T	Delft	SWEPOS C	60° 35'	17° 16'	75.4	
			95/02/07			Type A					
			95/08/01	Z-XII							
			96/05/07			Type B					
Norrköping		S	93/08/01	8000	DM Ash	Delft	SWEPOS	58° 35'	16° 15'	41.0	
			95/05/15			Type A					
			95/08/01	Z-XII							
			95/10/06		*						
			96/07/12								
			96/11/09			None					
						Type B					
Oikiluoto		F	94/10/19	8100	DM T	Delft	2 m CP	61° 14'	21° 28'	30.5	
			95/04/19	Z-XII							
Onsala		S	93/07/01	8000	DM B	Delft	IGS	57° 24'	11° 56'	45.5	
			93/08/16		*						
			95/05/20		*						
Oskarshamn		S	93/08/01	8000	DM Ash	Delft	SWEPOS	57° 04'	15° 60'	149.8	
			95/05/18		*						
			95/06/13			Type A					
			95/08/01	Z-XII							
			96/06/29			None					
			96/11/11			Type B					
Oulu		F	95/09/16	Z-XII	DM Ash	Ash	8 m IS	65° 05'	25° 54'	79.5	
Romuvaara		F	96/05/07	Z-XII	DM Ash	Ash	2 m CP	64° 13'	29° 56'	241.7	
Skellefteå		S	93/08/01	8000	DM T	Delft	SWEPOS	64° 53'	21° 03'	81.2	
			93/08/15		*						
			95/02/24			Type A					
			95/06/15		*						
			95/08/01	Z-XII							
			96/07/03			None					
			96/11/12			Type B					
Sodankylä	10513M001	F	94/08/14	8100	DM T	Delft	2.5 m SG	67° 25'	26° 23'	299.8	
			95/05/15	Z-XII							
Sundsvall		S	93/08/01	8000	DM T	Delft	SWEPOS	62° 14'	17° 40'	31.8	
			95/02/06			Type A					
			95/06/13		*						
			95/08/01	Z-XII							
			96/07/01			None					
			96/11/04			Type B					
Sveg		S	93/08/01	8000	DM T	Delft	SWEPOS	62° 01'	14° 42'	491.2	
			95/01/31			Type A					
			95/06/21		*						
			95/08/01	Z-XII							
			96/07/01			None					
			96/10/26			Type B					
Tuorla		F	94/08/15	8100	DM T	None	2.5 m SG	60° 25'	22° 27'	60.5	
			95/01/21	Z-XII							
Umeå		S	93/08/01	8000	DM T	Delft	SWEPOS	63° 35'	19° 31'	54.5	
			95/02/05			Type A					
			95/06/14		*						
			95/08/01	Z-XII							

			96/08/13				None			
			96/11/03				Type B			
Vaasa	10511M001	F	95/04/07	Z-XII	DM Ash	Ash	2.5 m SG	62° 58'	21° 46'	58.0
Vilhelmina		S	93/08/01	8000	DM T	Delft	SWEPOS	64° 42'	16° 34'	450.0
			95/02/02			Type A				
			95/06/18		*					
			95/08/01	Z-XII						
			96/06/28			None				
			96/10/27			Type B				
Virolahti		F	94/08/15	8100	DM T	Delft	2.5 m SG	60° 32'	27° 33'	36.9
			95/03/24	Z-XII						
Visby		S	93/08/01	8000	DM T	Delft	SWEPOS	57° 39'	18° 22'	79.8
			95/06/14			Type A				
			95/08/01	Z-XII						
			96/06/25			None				
			96/11/08			Type B				
Vänernborg		S	93/08/01	8000	DM T	Delft	SWEPOS	58° 42'	12° 02'	169.7
			93/09/09		*					
			95/05/22		*					
			95/06/24			Type A				
			95/08/01	Z-XII						
			96/05/23			None				
			96/11/13			Type B				
Östersund		S	93/08/01	8000	DM T	Delft	SWEPOS	63° 27'	14° 51'	490.1
			95/02/01			Type A				
			95/08/01	Z-XII						
			95/09/15		*					
			96/07/08			None				
			96/10/27			Type B				
Överkalix		S	93/08/01	8000	DM Ash	Delft	SWEPOS	66° 19'	22° 46'	223.0
			94/06/15		*					
			95/06/16		*					
			95/07/10			Type A				
			95/08/01	Z-XII						
			96/06/28			None				
			96/11/01			Type B				

<sup>a</sup>WGS-84 ellipsoidal coordinates.

<sup>b</sup>The DOMES number is a unique station identifier issued by the International Earth Rotation Service. Only some of the SWEPOS sites have been so registered.

<sup>c</sup>S = SWEPOS, F = FinnRef.

<sup>d</sup>8000 = AOA SNR-8000; 8100 = AOA SNR-8100; Z-XII = Ashtec Z-XII.

<sup>e</sup>Variants of the Dorne-Margolin (DM) choking GPS antenna have been used, including the DM-B, the DM-T, and the Ashtec manufactured version denoted "DM Ash." An asterisk indicates that the antenna was removed and replaced.

<sup>f</sup>See text and *Emardson et al.* [2000].

<sup>g</sup>SWEPOS Monuments are denoted as "SWEPOS" for standard, and variants "B" and "C" (see text). IGS is the Onsala mount (see text). SG = Steel Grid Mast, CP = Concrete Pillar, IS = Invar Stabilized.

**Table 2.** Site velocities in ITRF96.

Site	Velocity Estimates, mm yr <sup>-1</sup>						
	Standard Solution			Edited Solution			EOF Solution
	East	North	Up	East	North	Up	Up
Arjeplog	-1.5±0.1	1.4±0.1	10.2±0.8	-2.0±0.3	1.4±0.2	10.1±0.8	9.2±2.3
Borås	-2.0±0.2	-0.1±0.1	1.5±1.1	-2.0±0.5	-0.1±0.3	2.9±1.3	
Hässleholm	1.0±0.1	0.3±0.1	2.6±0.6	-0.3±0.2	-0.8±0.1	-1.5±0.6	3.4±1.3
Joensuu	1.7±0.2	-0.6±0.1	-1.5±0.4	1.1±0.2	-0.4±0.1	-1.1±0.5	
Jönköping	1.1±0.1	-0.2±0.1	0.7±0.8	-2.3±0.3	-0.8±0.2	0.2±0.9	1.7±1.7
Karlstad	-0.5±0.1	-0.5±0.1	4.3±0.6	-1.4±0.3	-0.4±0.1	2.9±0.7	4.1±1.3
Kevo	1.8±0.3	1.7±0.2	-3.5±1.1	2.1±0.3	1.5±0.2	-0.7±1.1	
Kiruna	0.3±0.1	1.5±0.1	11.7±0.9	0.3±0.3	-0.3±0.2	4.7±0.9	10.6±1.9
Kivetty	-1.3±0.4	-0.8±0.2	5.5±1.0	0.2±0.4	-0.8±0.2	3.2±1.0	
Kuusamo	2.9±0.5	-0.2±0.3	8.8±1.4	2.9±0.5	-0.4±0.3	2.9±1.6	
Leksand	-0.1±0.1	0.7±0.1	5.1±0.7	-1.5±0.4	0.2±0.2	4.6±1.0	5.2±1.8
Lovö	1.5±0.1	-0.7±0.1	1.5±0.9	-0.8±0.4	-0.4±0.2	0.6±1.0	
Metsähovi	0.1±0.1	-1.5±0.1	2.1±0.7	-0.3±0.1	-1.6±0.0	1.4±0.2	3.7±1.4
Mårtsbo	-0.7±0.1	-0.3±0.1	6.5±0.6	-0.5±0.2	-1.0±0.1	6.0±0.6	5.7±1.4
Norrköping	1.7±0.1	-0.8±0.1	3.2±0.9	-0.6±0.4	-0.8±0.2	1.9±1.0	
Olkiluoto	1.9±0.2	-1.0±0.1	7.5±0.5	1.4±0.2	-0.6±0.1	7.0±0.5	
Onsala	-0.2±0.1	-0.4±0.1	0.1±0.8	-1.4±0.3	-0.4±0.1	-1.0±0.7	0.3±1.5
Oskarshamn	1.1±0.1	0.8±0.1	1.1±0.9	-1.6±0.4	-0.3±0.2	-0.8±1.0	
Oulu	0.7±0.2	0.2±0.1	5.9±0.6	1.2±0.2	0.2±0.1	3.7±0.6	
Romuvaara	-0.2±0.5	-1.5±0.3	7.7±1.5	-1.8±0.6	-0.9±0.3	11.4±1.6	
Skellefteå	-0.3±0.1	0.1±0.1	9.8±0.8	0.2±0.3	-0.1±0.2	8.1±0.9	10.7±1.6
Sodankylä	1.2±0.2	0.6±0.1	6.1±0.5	1.2±0.2	0.6±0.1	6.5±0.6	
Sundsvall	-1.4±0.1	0.1±0.1	8.6±0.6	-1.9±0.3	-0.3±0.1	7.2±0.7	8.8±1.6
Sveg	-0.4±0.1	0.2±0.1	7.5±0.6	-1.7±0.3	-0.1±0.1	7.7±0.7	9.9±1.6
Tromsø	-1.8±0.1	1.5±0.1	-0.8±0.3	-1.5±0.1	1.7±0.1	-0.7±0.3	
Tuorla	1.3±0.2	-0.6±0.1	2.7±0.5	1.3±0.2	-0.6±0.1	3.4±0.5	
Umeå	-0.2±0.1	0.1±0.1	10.1±0.6	-1.1±0.3	-0.9±0.2	9.2±0.7	10.9±1.6
Vaasa	0.8±0.2	-0.6±0.1	8.8±0.5	0.4±0.2	-0.4±0.1	8.4±0.5	
Vilhelmina	-1.5±0.1	0.8±0.1	6.4±0.6	-2.1±0.3	0.0±0.2	5.4±0.7	7.3±1.6
Virolahti	0.3±0.3	-1.2±0.2	0.3±0.9	0.9±0.2	-0.8±0.1	-1.1±0.4	
Visby	-0.8±0.1	-0.8±0.1	2.0±0.6	-1.3±0.2	-1.7±0.1	-0.9±0.6	1.8±1.3
Vänernborg	-0.7±0.1	-0.3±0.1	2.9±1.0	-1.3±0.4	0.2±0.2	6.0±1.0	4.8±2.1
Östersund	-0.6±0.1	0.5±0.1	6.3±0.7	-2.3±0.2	0.1±0.1	7.9±0.6	7.6±1.7
Överkalix	-0.1±0.1	2.1±0.1	2.9±0.9	1.8±0.3	1.7±0.2	4.5±1.0	7.7±2.0

The uncertainties shown are the standard errors (see text).

**Table 3.** Tidal loading effects.

Effect	Assumed Amplitude, <sup>†</sup> mm	Example Sites	Calculated Admittance	Total Amplitude, mm
(a) Snow, soil moisture	300	Inland sites Coastal sites	-0.035 -0.021	-10 -6
(b) Kattegatt water level	±500	Onsala Vänernborg <sup>‡</sup>	-0.015 -0.005	±8 ±2
(c) Baltic water level	±500	Visby Oskarshamn Finnish sites	-0.020 -0.016 -0.012	±10 ±8 ±6
(d) Great lake water level	±10 <sup>3</sup>	Karlstad Jönköping	-0.004 -0.003	±4 ±3
(e) Hydropower lake water level	±10 <sup>4</sup>	Coastal sites Other sites	-0.001 30%(?)	±10 ±(3-5)

<sup>†</sup>Estimated from various sources.

<sup>‡</sup>Also Hässleholm.

**Table 4.** Pillar measurements.

Pillar	Date	Reference Position*		
		North, mm	East, mm	Up, mm
Arjeplog	93/08/16	-0.164	0.208	458437.694
Kiruna	93/08/17	4574.341	-4558.030	2900.038
	94/06/15	4574.454	-4558.301	2900.163
	94/06/15	4574.249	-4557.917	2900.015
	95/06/16	4574.347	-4558.288	2900.452
Skellefteå N	93/08/15	-0.366	0.434	58916.931
	95/06/15	-0.612	0.249	58916.984
Skellefteå S	93/08/15	0.817	1.487	58941.716
	95/06/15	1.107	-0.139	58942.120
Hässleholm	93/06/14	0.001	-0.001	78509.726
	95/05/19	-0.012	-0.220	78509.310
Jönköping	93/06/18	0.006	0.039	227368.024
	94/06/23	0.028	-0.070	227367.941
	94/06/23	0.002	-0.151	227367.891
	95/05/21	-0.186	-0.233	227368.054
Karlstad	93/08/12	-0.200	0.026	82786.824
	95/05/23	0.042	0.563	82786.121
Leksand	93/08/11	-0.264	-0.253	447573.368
	94/01/18	-0.278	0.063	447572.154
	94/01/18	-0.276	0.121	447572.182
	94/02/06	-0.327	0.145	447572.615
	94/02/06	-0.335	0.114	447572.491
	94/03/08	-0.428	0.097	447572.502
	94/03/08	-0.431	0.158	447572.462
	94/04/15	-0.576	0.218	447572.577
	94/04/15	-0.590	0.176	447572.433
	94/06/14	-0.421	-0.336	447572.718
	94/08/25	0.252	-0.357	447572.786
	94/08/25	0.263	-0.304	447572.767
	95/10/05	-0.363	0.146	447572.943
Mårtsbo N	93/08/05	0.656	0.778	50551.547
	95/10/06	0.098	0.570	50550.558

**Table 4.** (continued)

Pillar	Date	Reference Position*		
		North, mm	East, mm	Up, mm
Mårtsbo S	93/08/05	-1708.119	6.033	50546.508
	95/10/06	-1707.842	5.270	50545.648
Lovö	93/10/28	-0.537	-0.499	56086.280
	95/05/16	-0.532	-0.215	56086.310
Norrköping	93/08/22	-0.074	-0.046	12870.190
	94/06/29	0.540	0.481	12870.061
	94/06/29	0.425	0.308	12869.927
	95/05/17	0.286	0.303	12869.456
Onsala	93/08/16	-216.580	-171.680	10039.377
	95/05/20	-216.127	-171.758	10039.511
Oskarshamn	93/06/16	-0.062	0.017	119433.397
	95/05/18	-0.170	-0.221	119432.693
Sundsvall	93/08/09	-0.091	-0.300	7094.946
	95/06/13	0.754	-1.390	7094.823
Sveg	93/08/03	0.029	-0.012	458203.058
	95/06/21	-0.040	0.077	458203.043
Umeå	93/06/13	0.000	0.003	31531.774
	95/06/14	-0.544	-0.665	31534.045
Vilhelmina	93/08/11	0.043	-0.063	420142.000
	95/06/18	-0.394	0.951	420141.126
Visby	93/08/12	-1.866	1.323	54864.592
	93/08/12	-1.514	1.154	54863.358
Vänernborg	93/09/09	0.376	0.605	134762.710
	95/05/22	0.092	0.975	134762.404
Östersund	93/08/10	-1.045	0.285	458386.234
	95/09/15	-0.19	0.009	458386.585
Överkalix	94/06/15	0.517	0.413	200290.683
	94/06/15	0.474	0.301	200290.535
	95/06/16	0.472	1.064	200290.406

\*Heights in the Swedish national height system. Northing and easting in local reference system established at each site.

**Figure 1.** Map showing GPS sites used in the study. Subnetworks are indicated by the symbols used: SWEPOS (triangles) and FinnRef (circles). IGS sites are indicated by diamonds. The Kiruna IGS site, located close to the Kiruna SWEPOS site, is not shown. The Onsala and Metsähovi sites are also IGS sites.

**Figure 2.** Time series of site positions for the BIFROST sites and Tromsø from the Standard Solution. Shown in blue are differences in mm from a series mean for the east (left column), north (middle), and radial (right) components of site position. The red line shows the model fit to the time series, and the yellow vertical lines indicate epochs at which an offset was introduced.

**Figure 3.** Comparison between Standard, Edited, and EOF solutions.

**Figure 4.** (a) Vertical crustal rates from GIA predictions calculated using a method outlined in the text. (b) Simple Gaussian model produced by a least-squares fit to the observed GPS vertical crustal rates.

**Figure 5.** Comparison between the rates observed from the GPS data and those predicted by the Earth/ice model combination discussed in the text for the (a) east, (b) north, and (c) radial components of velocity.

**Figure 6.** Observed sea-level rates from Baltic tide gauges versus negative crustal vertical rates obtained from the Gaussian model of Figure 5b. The mathematical relationship between these quantities is given in (2).

**Figure 7.** Residuals for radial component for Umeå from EOF analysis (a) first and (c) second stages, after the recycling of the (b) “common mode” based on the residuals for the network of sites. For clarity the error bars are not shown. The WRMS residuals are (a) 7 mm; (b) 4 mm, and (c) 3 mm.

**Figure 8.** Eigenvectors in model space. The signal channels through which residuals at neighbor stations have been recycled are numbered 15–25. The associated GPS stations are, in order of their parameter number, Metsähovi, Skellefteå, Umeå, Sundsvall, Mårtsbo, Leksand, Sveg, Östersund, Vilhelmina, Arjeplog, and Kiruna. The residuals contribute to the set of signals from which the (orthonormal) eigenvectors are constructed. Eigenvector number 01 conveys a common mode of the recycled noise. Deleting from the model space all eigenvectors that convey the residual information except the one that is associated with the largest eigenvalue constitutes the extended EOF method used in this paper.

**Figure 9.** Correlation between vertical time series from pairs of GPS sites as a function of intersite line length. The smaller “branch” at a correlation of  $\sim 0.2$  contains correlations with site Metsähovi. This site was used to establish the reference frame, so the correlated variations in position might have been removed to a greater extent.

**Figure 10.** Examples of power spectra for the three components of position for six sites. The dotted line indicates the 95% confidence level for white noise errors whose standard deviations are given by the standard errors for the position estimates.

**Figure 11.** Time series of the pillar measurements for the Leksand site. The error bars are equal to the RMS based on the repeated measurements from other sites (see text). The symbols represent the different components of position: square with solid line, north; circle with dashed line, east; and triangle with short dashed line, up. Each of the time series have been de-meant, and slightly offset in the abscissa for clarity.

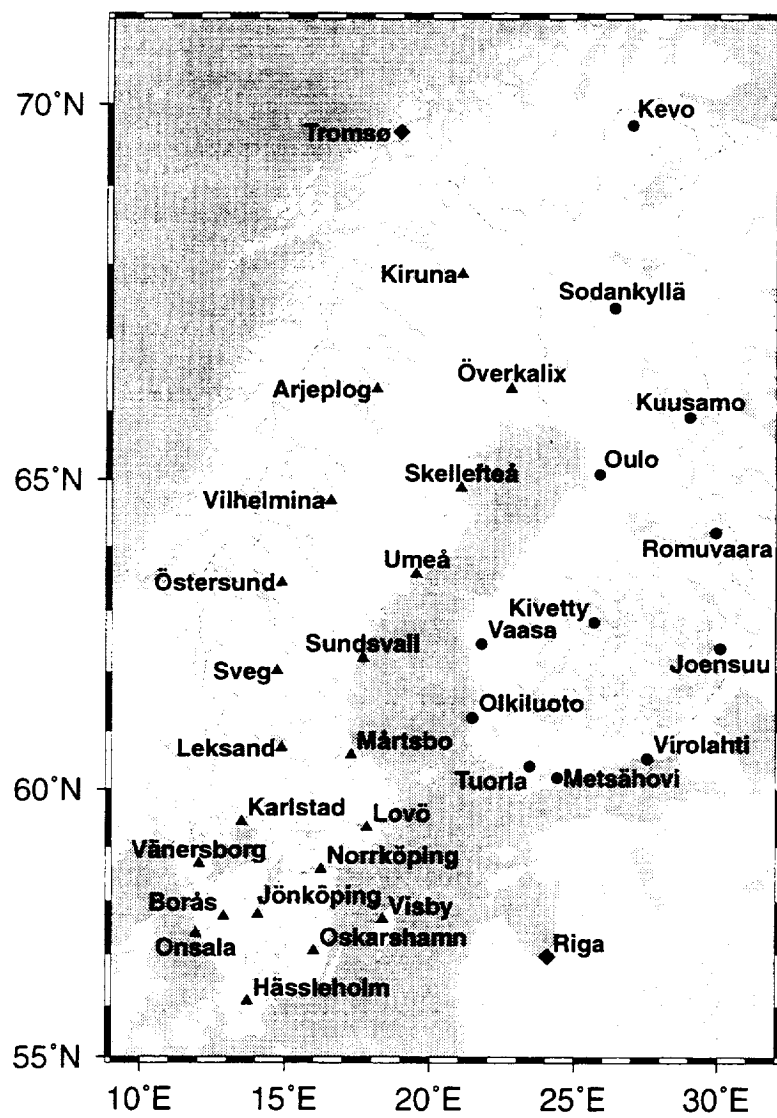


Figure 1

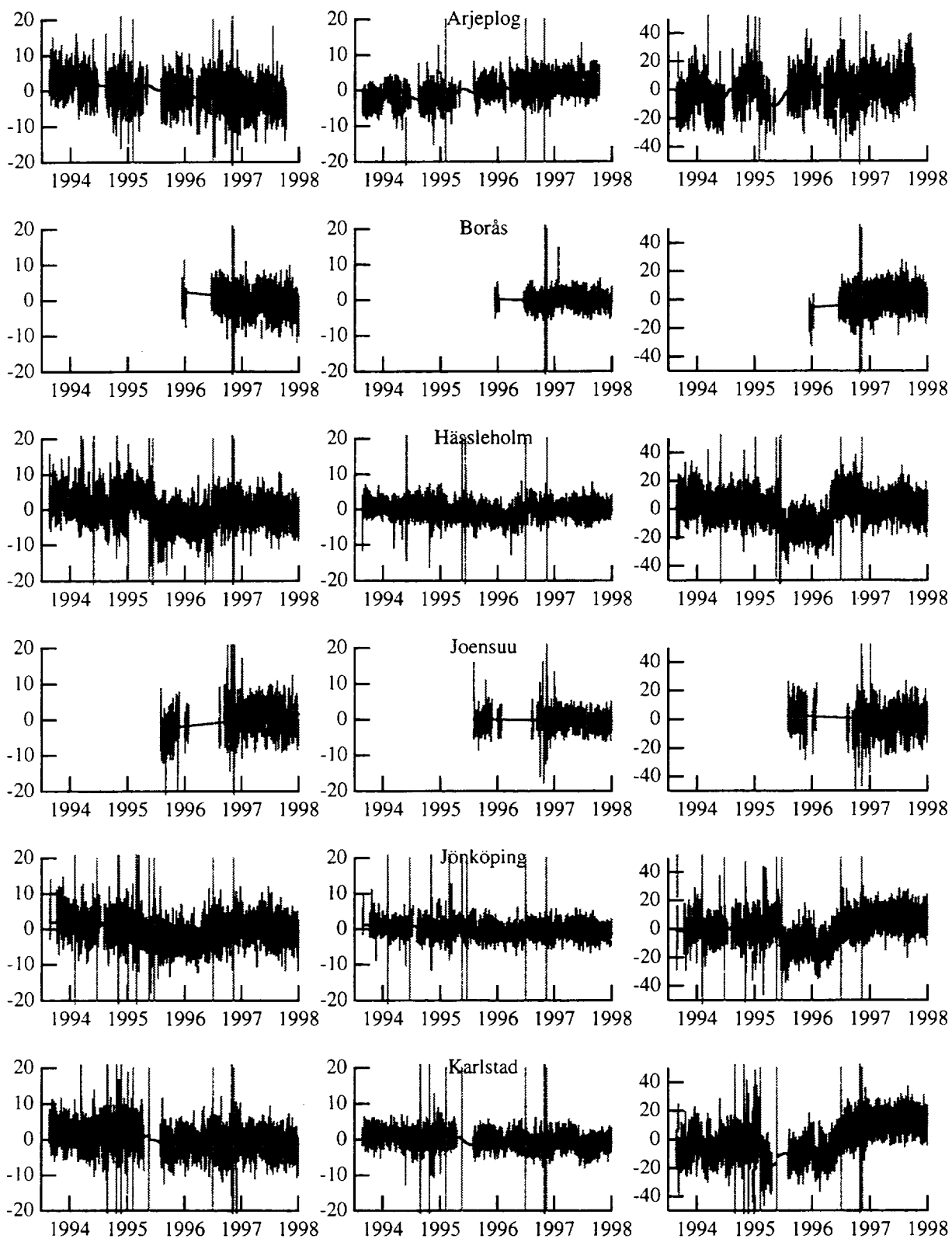


Figure 2

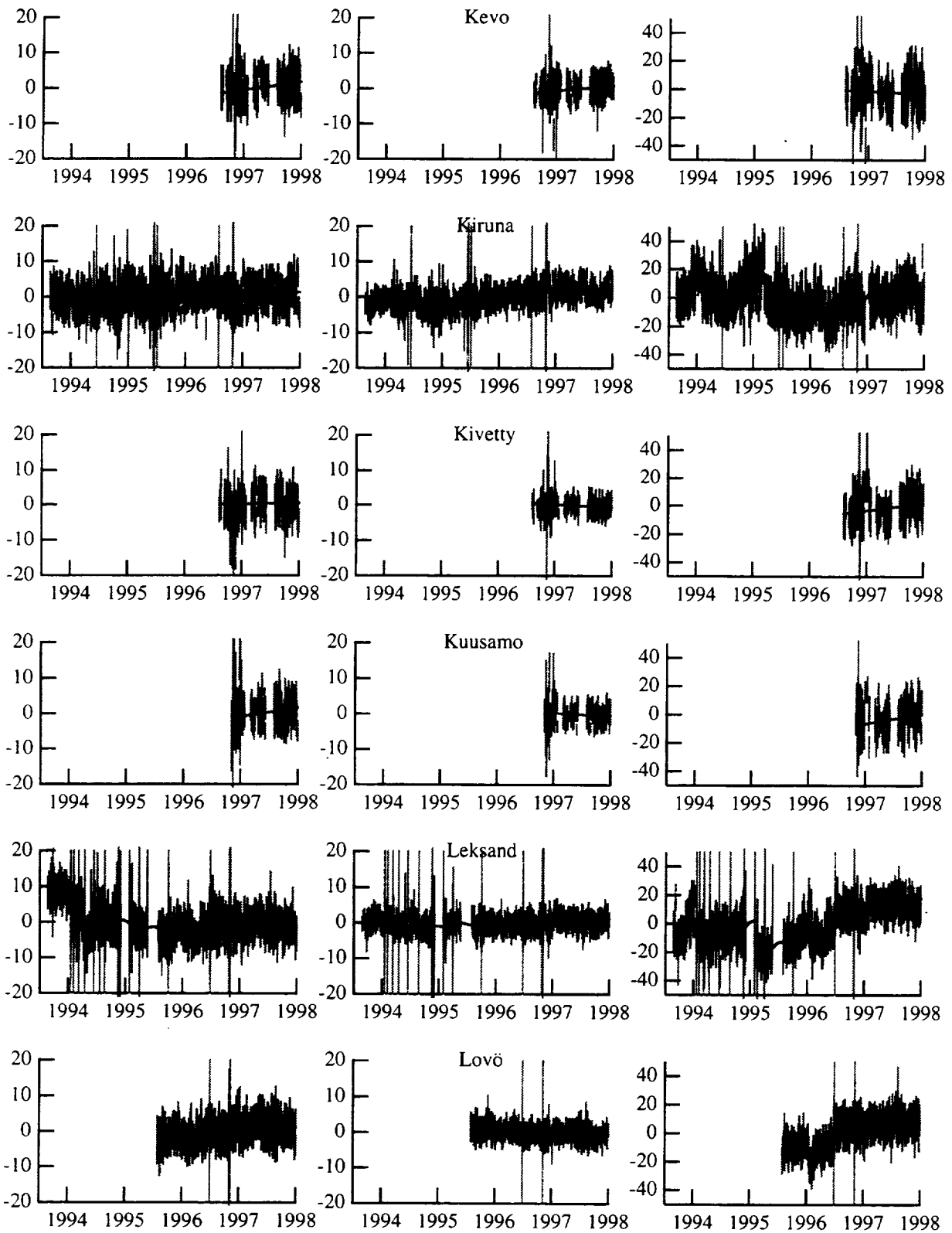


Figure 2 (continued)

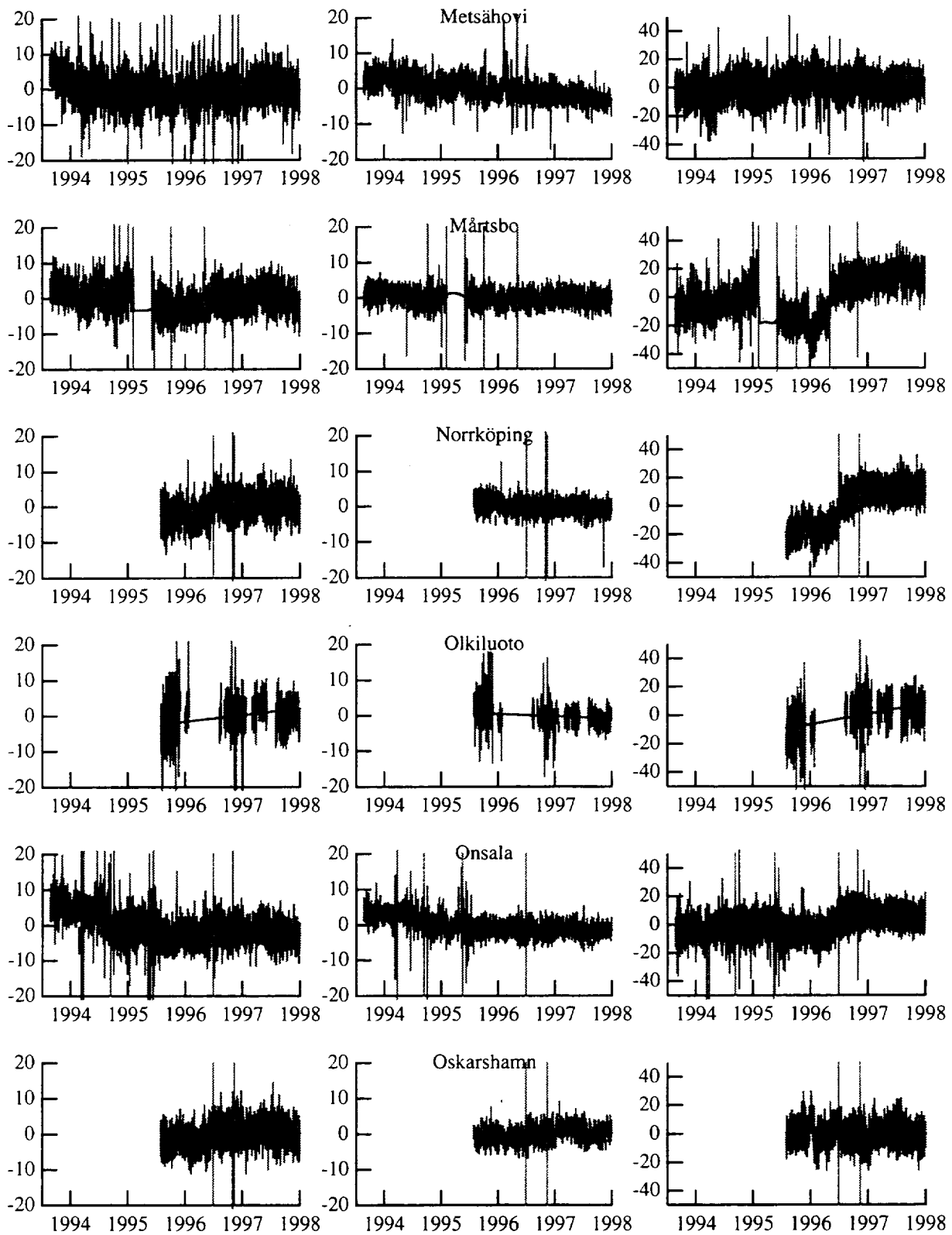


Figure 2 (continued)

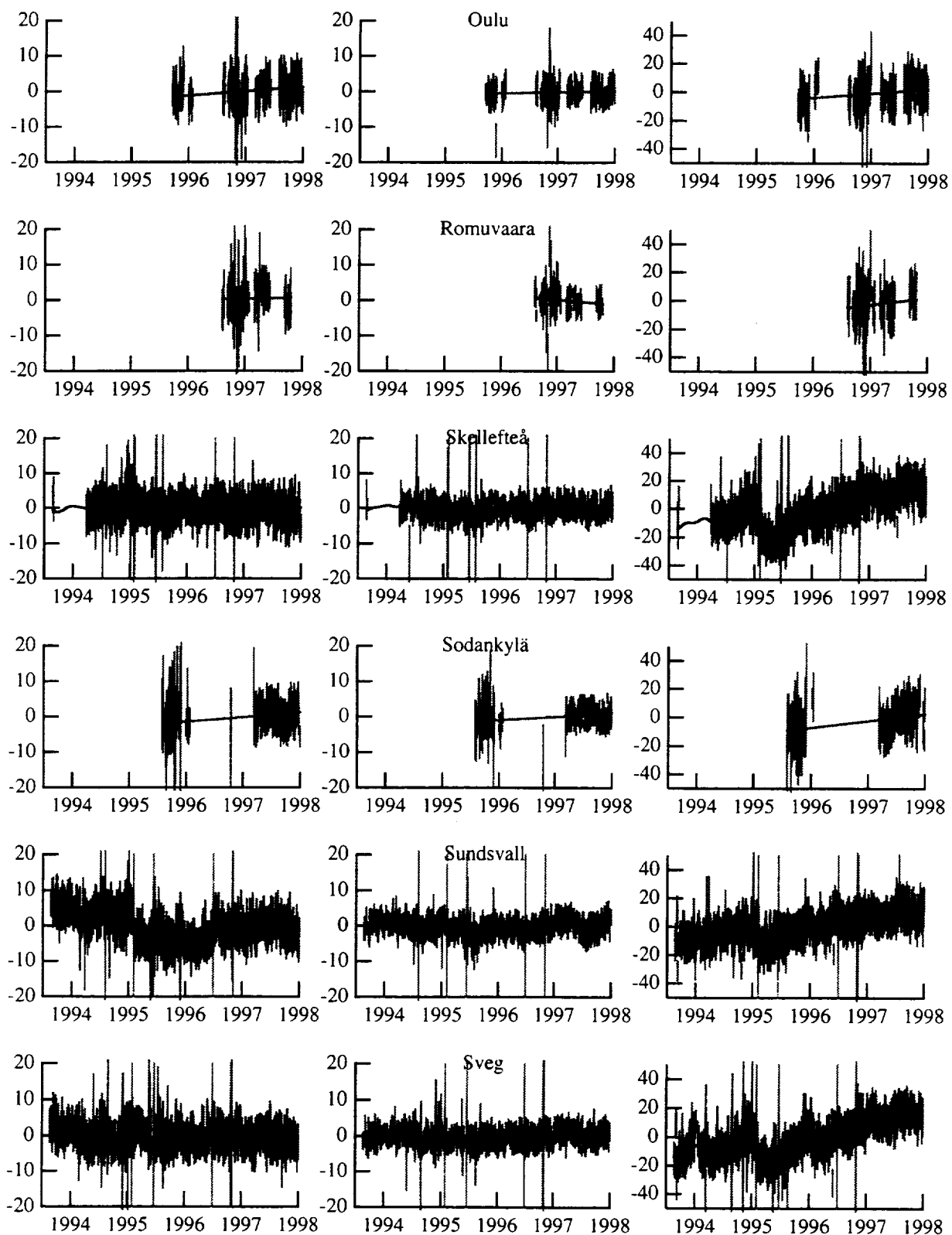


Figure 2 (continued)

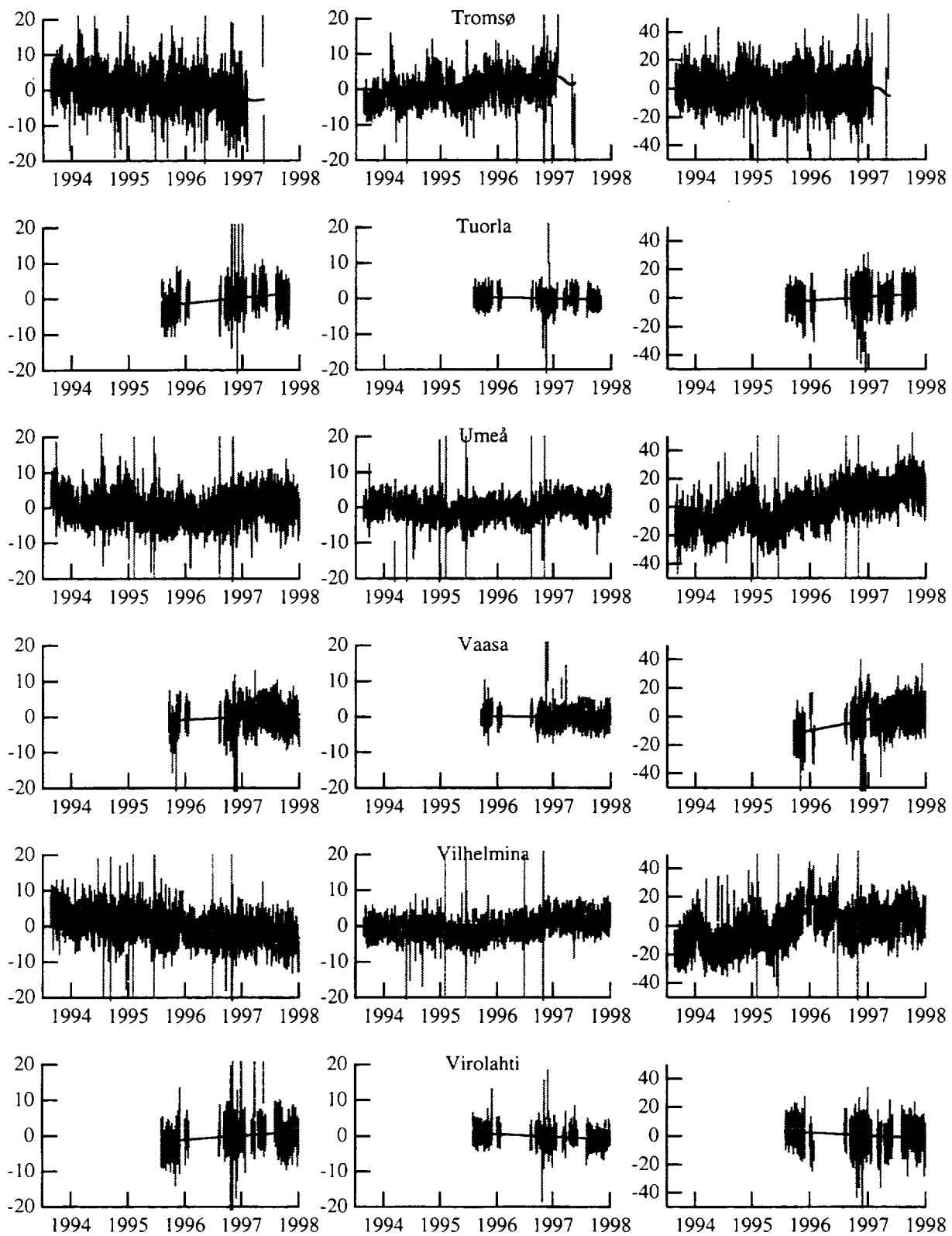


Figure 2 (continued)

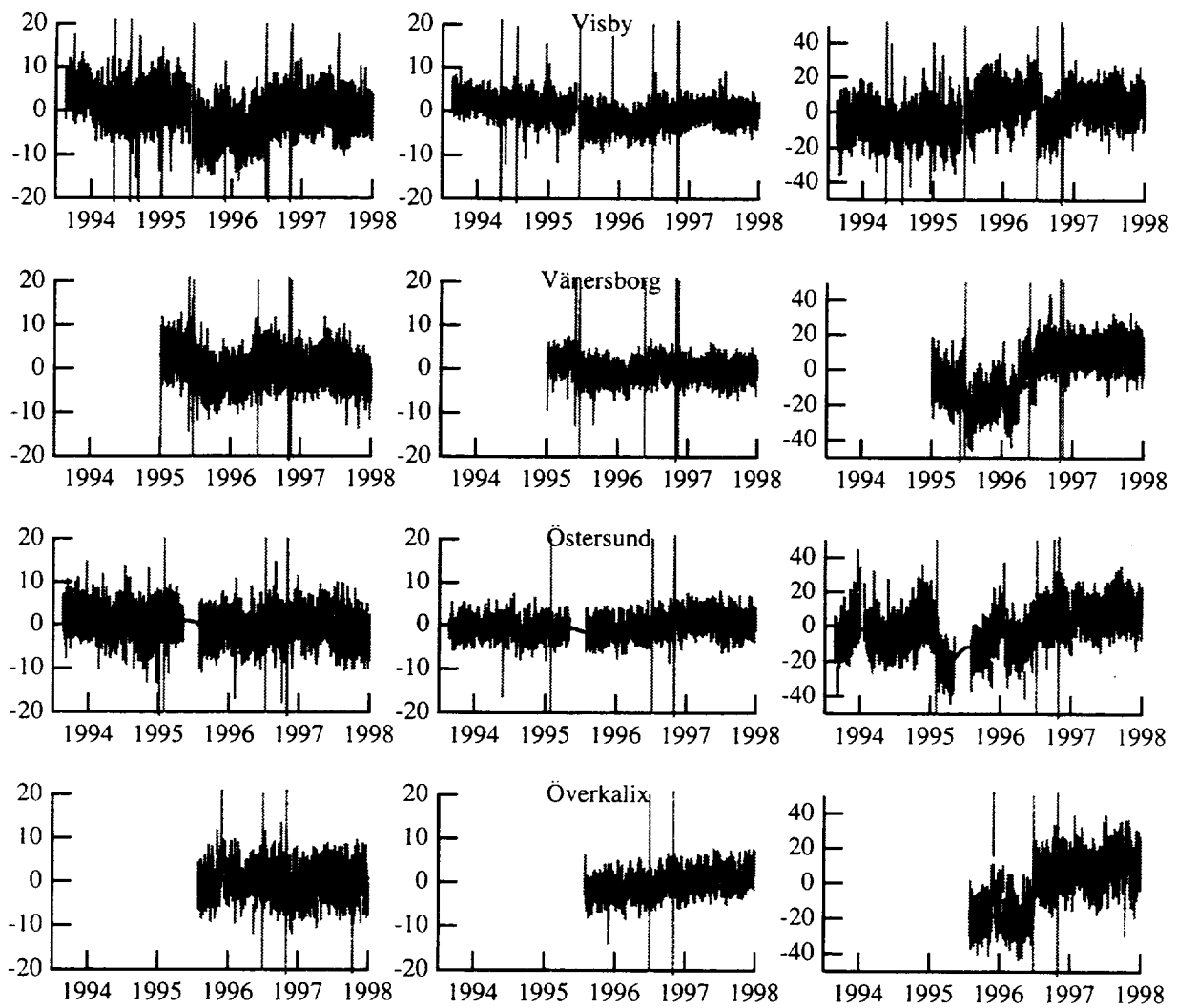


Figure 2 (continued)

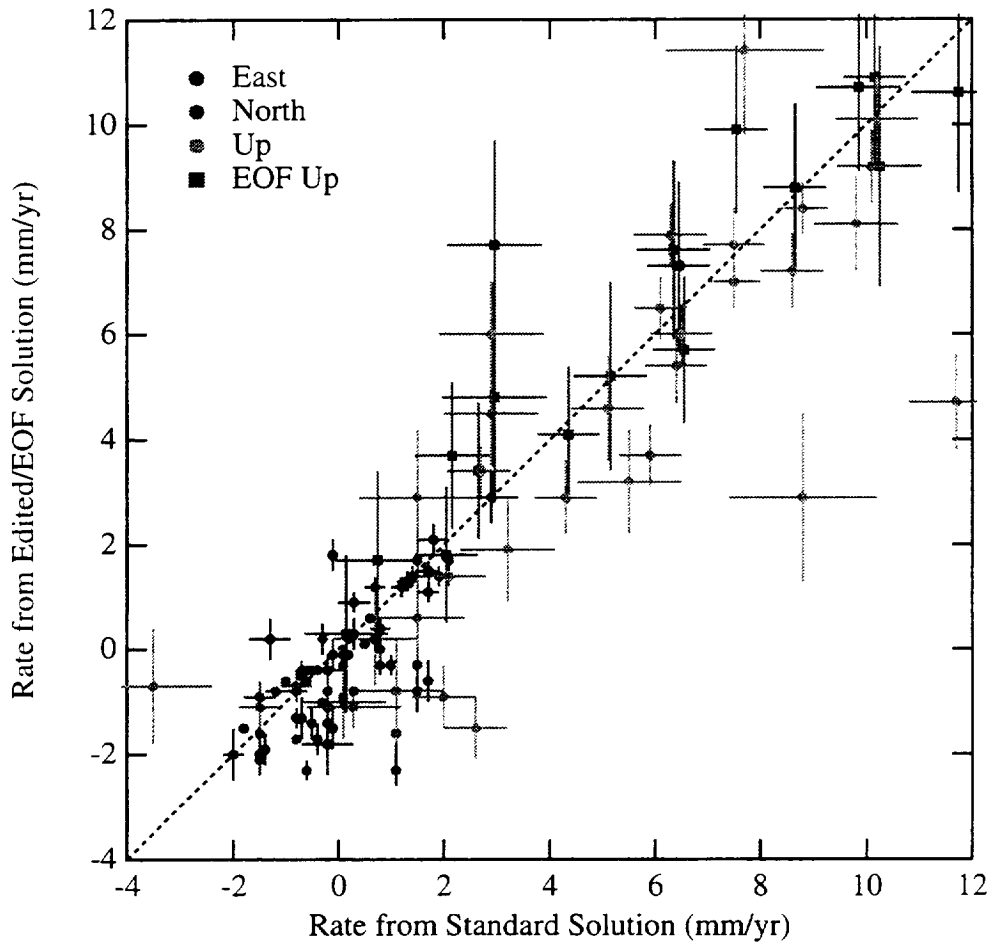


Figure 3

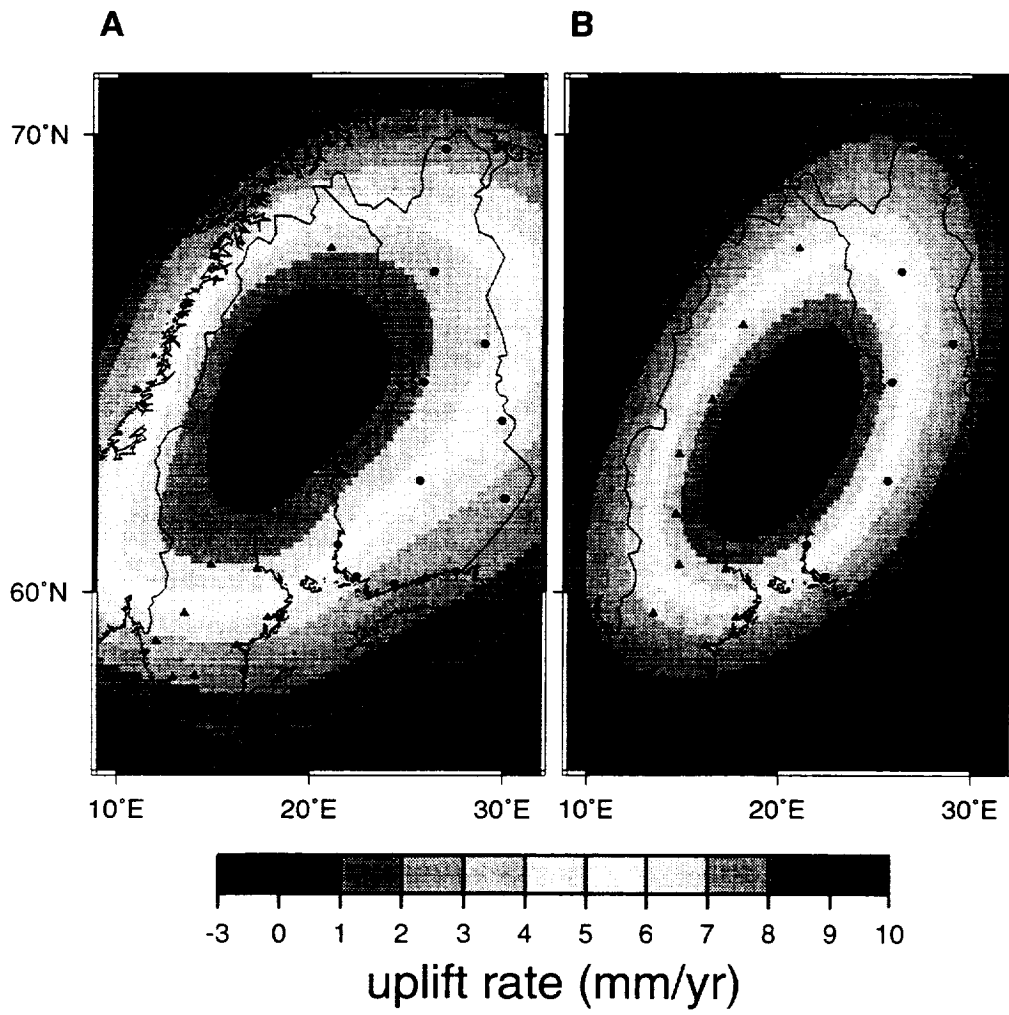


Figure 4

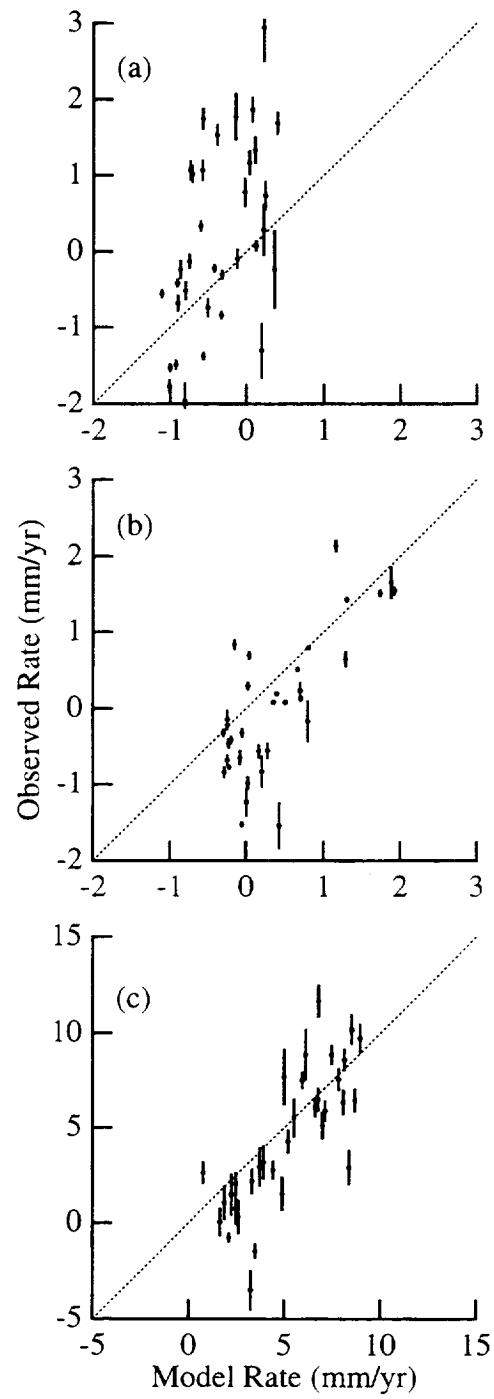


Figure 5

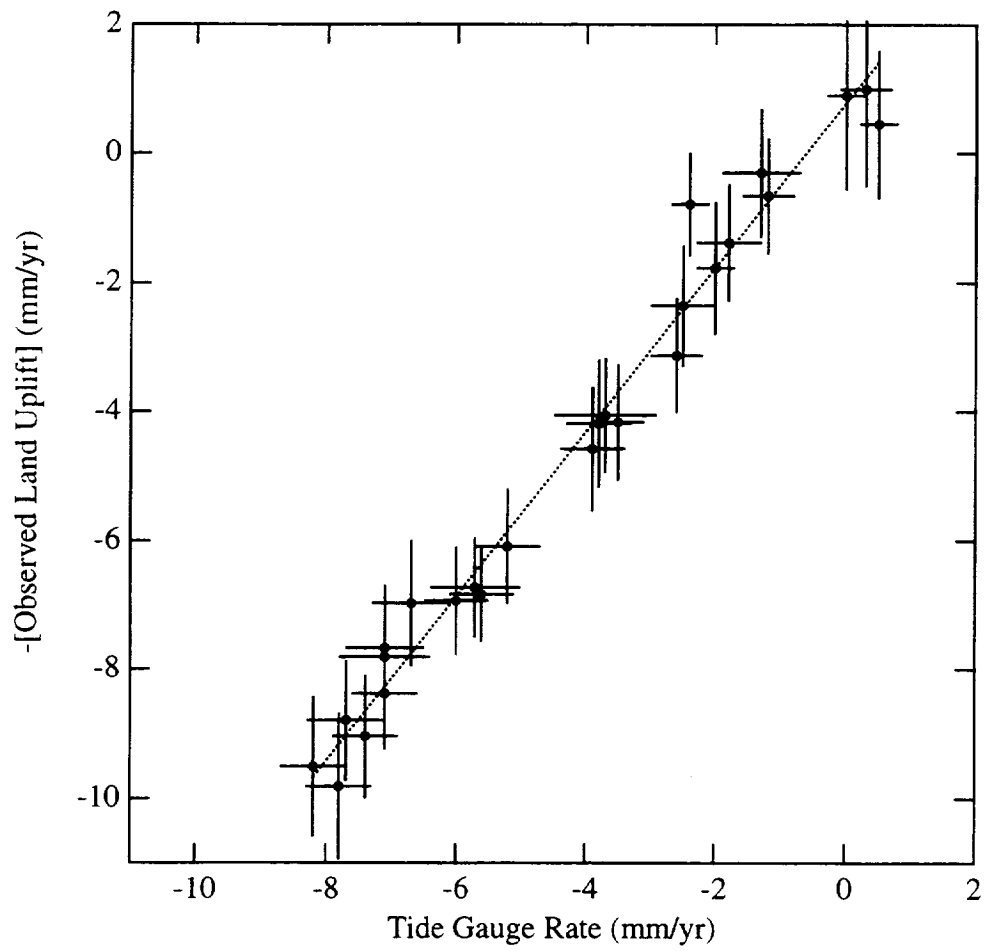


Figure 6

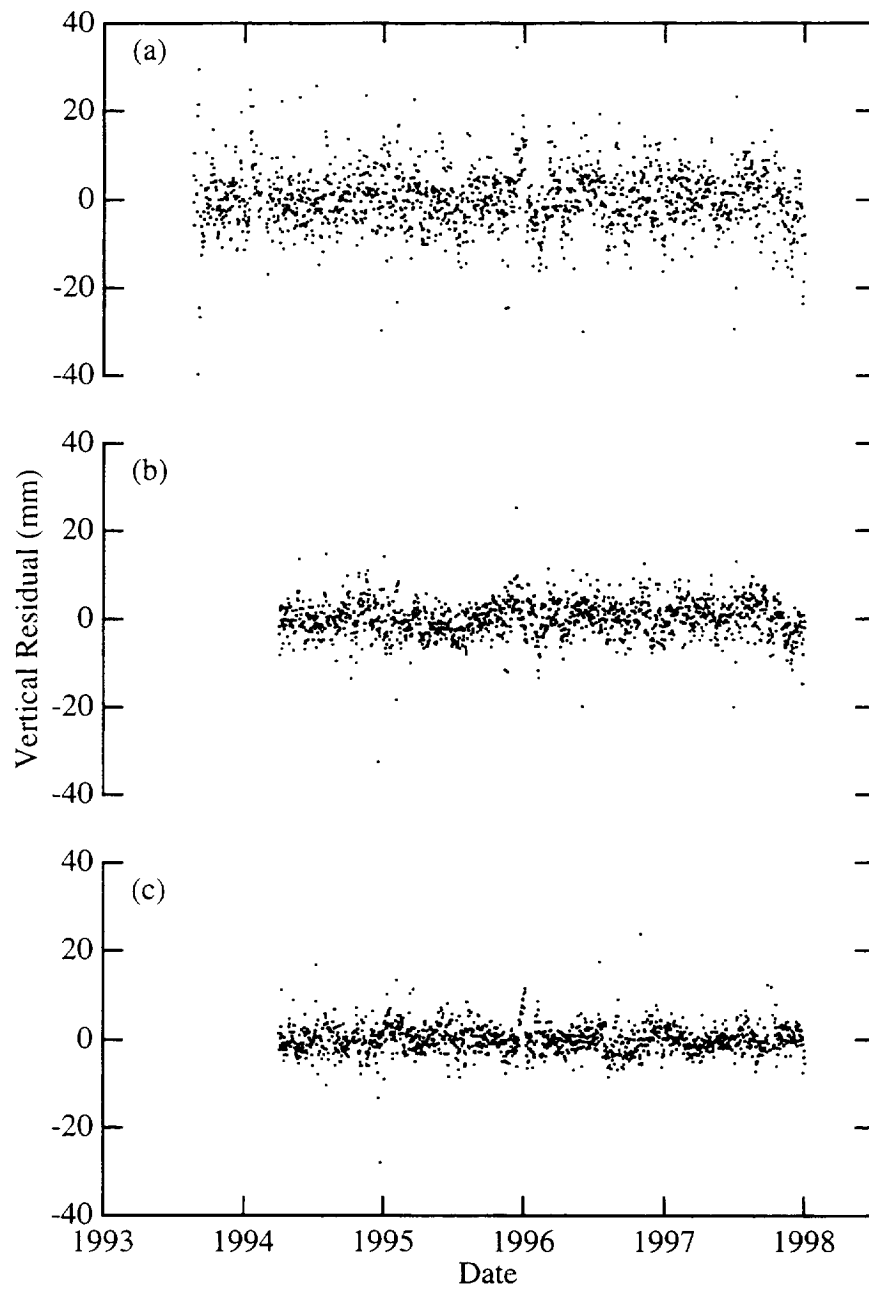


Figure 7

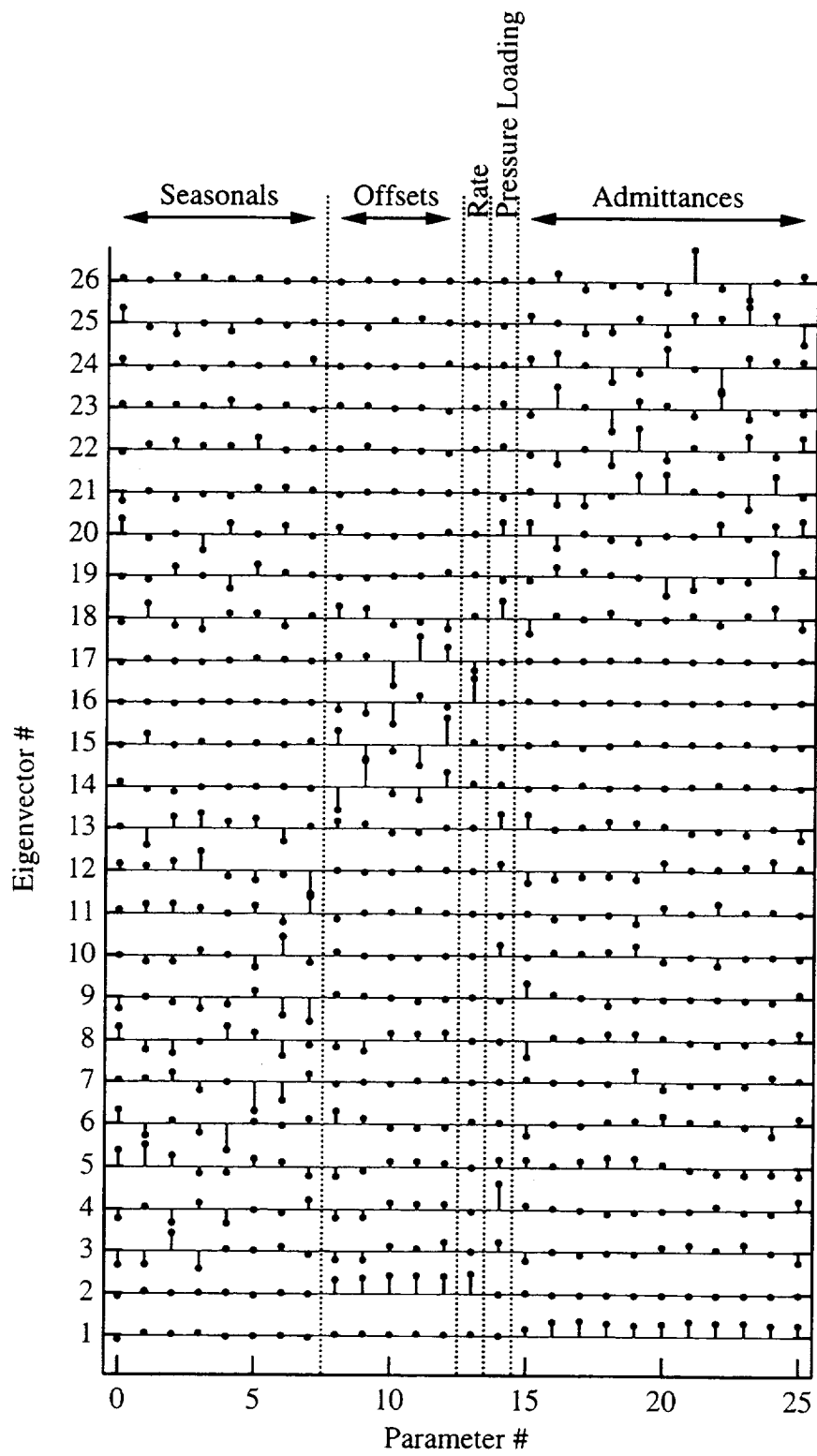


Figure 8

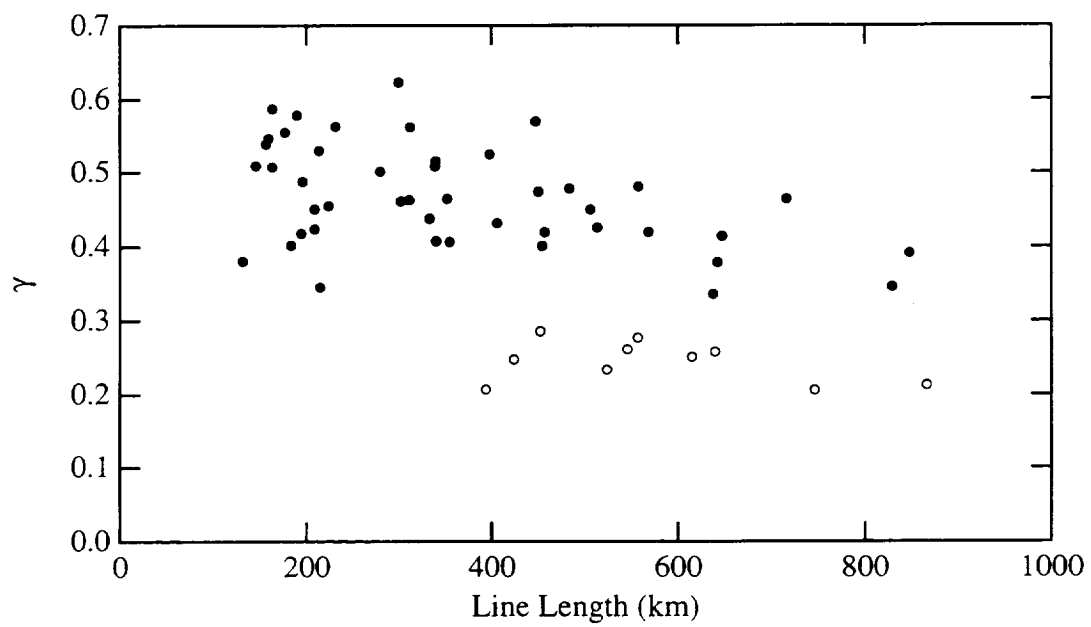


Figure 9

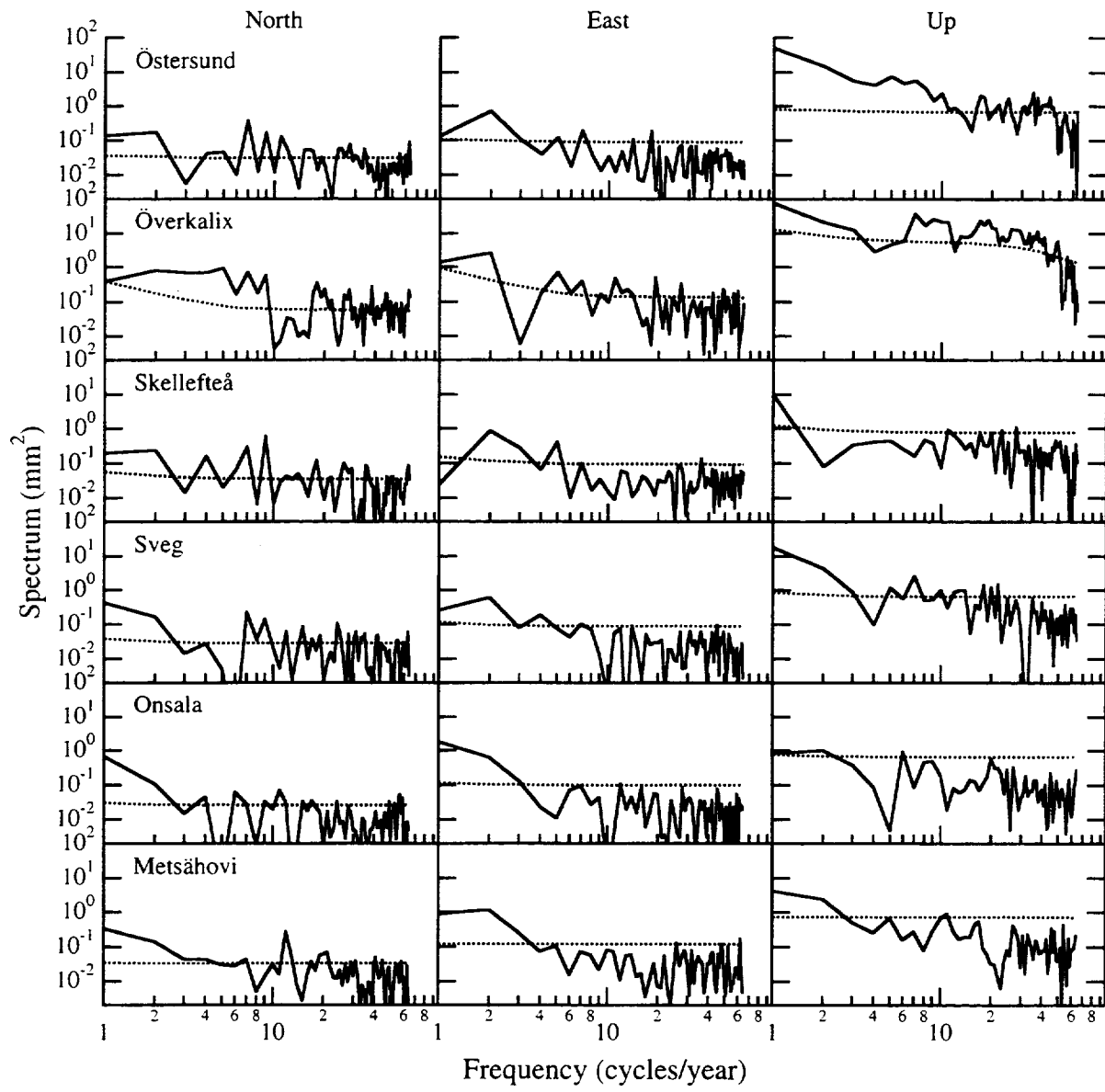


Figure 10

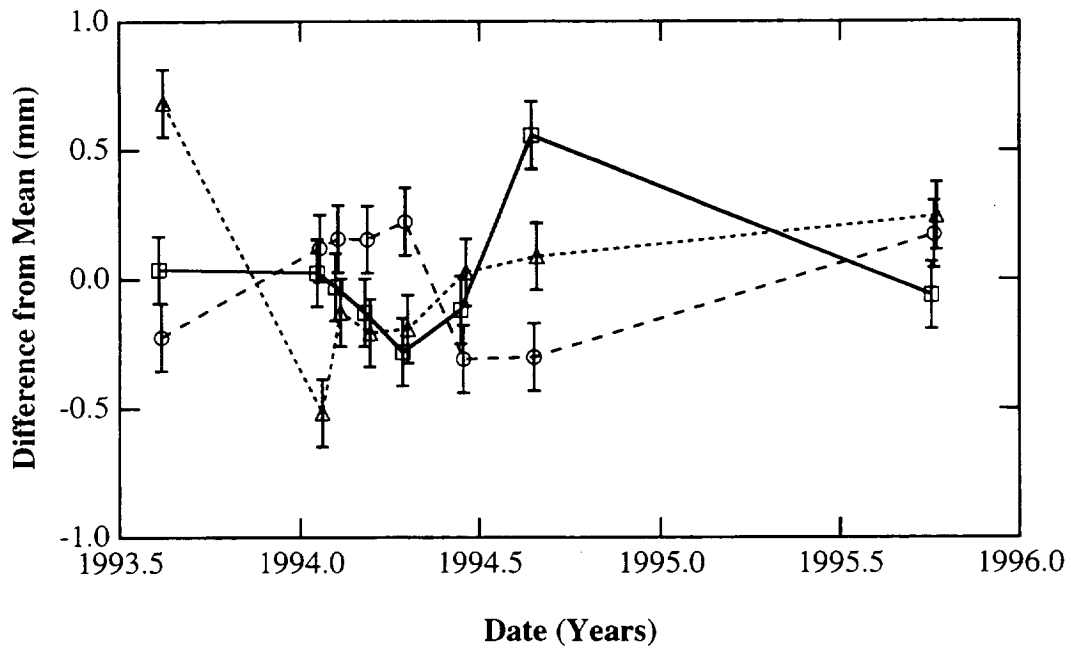


Figure 11

